Marine and Petroleum Geology 162 (2024) 106694

Contents lists available at ScienceDirect

Marine and Petroleum Geology

journal homepage: www.elsevier.com/locate/marpetgeo

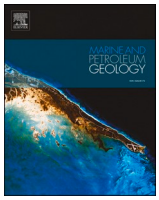

Characteristics and origin of crystalline dolomite: A case from Paleogene lacustrine fine-grained rocks in Jiyang depression, Bohai Bay Basin, China

Zhouhai Xiong [a,*], Yingchang Cao [a,b], Chao Liang [a]

[a] National Key Laboratory of Deep Oil and Gas, China University of Petroleum (East China), Qingdao, 266580, China
[b] Laboratory for Marine Mineral Resources, Qingdao National Laboratory for Marine Science and Technology, Qingdao, 266071, China

ARTICLE INFO

Keywords:
Fine-grained sedimentary rocks
Shale oil
Dolomite
Diagenesis

ABSTRACT

Crystalline dolomite is a common carbonate mineral in lacustrine fine-grained rocks, but it has a confusing origin that has been a focus of much debate in recent years. In our research, the fine-grained rocks rich in crystalline dolomite were sampled from the upper fourth member (UMbr 4) and lower third member (LMbr 3) of the Shahejie Formation in the Jiyang Depression, and analyzed by a variety of analytical techniques, including field emission scanning electron microscopy (FESEM), cathodoluminescence (CL), laser ablation inductively coupled plasma mass spectrometry (LA-ICP-MS), micro-area carbon, oxygen, strontium isotopes and electron probe analyses. The results show: ①The crystalline dolomites in the lacustrine fine-grained rocks are primarily composed of ferroan-poor dolomite (FeO < 1%), type I ferroan dolomite (FeO ≈ 5%) and type II ferroan dolomite (FeO ≈ 16%); ②The $\delta^{18}O$ of ferroan-poor dolomites in mudstone is between −0.89 and 0.32‰, the precipitation temperature is less than 60 °C, and their formation is related to the microbial action during the early diagenetic stage A, while the ferroan-poor dolomites in dolostone are primarily formed by the recrystallization of micritic dolomite; ③The $\delta^{18}O$ of type I ferroan dolomites ranges from −3.74 to −3.89‰, the precipitation temperature ranges from 68.4 to 69.4 °C, and they are primarily formed by the microbial action and clay mineral transformation during the early diagenetic stage B; ④The $\delta^{18}O$ of type II ferroan dolomites is between −7.78 and −8.33‰, the precipitation temperature is more than 90 °C, and their formation is related to the dissolution of early carbonate and clay mineral transformation during the middle diagenetic stage; ⑤The origin mechanism of crystalline dolomite indicates the diagenetic evolution of fine-grained rocks and the migration path and storage of shale oil.

1. Introduction

Since Deodal de Dolomieu, a French geologist, first described dolomite in 1791, scientists have been studying dolomite for more than 200 years (Mazzullo, 1992; He et al., 2010; Zhang et al., 2019a; Pan et al., 2022). Due to the complex geological factors of dolomite formation, researchers have demonstrated through experiments that it is difficult to directly synthesize dolomite at temperatures below 60 °C (Sibley et al., 1987; Land, 1998; Arvidson and Mackenzie, 1999; McKenzie and Vasconcelos, 2009; Kaczmarek and Thornton, 2017; Huang et al., 2019; Zhang et al., 2021). Many classical models of dolomite origin were proposed early, such as evaporative dolomitization model (Shinn et al., 1965; Friedman and Sanders, 1967; Hsü and Siegenthaler, 1969), seepage-reflux model (Adams and Rhodes, 1960; Deffeyes et al., 1965), mixed-zone dolomitization model (Badiozamani, 1973), seawater dolomitization model (Land, 1985; Burns and Baker, 1987; Carballo et al., 1987; Vahrenkamp et al., 1994), burial dolomitization model (Mattes and Mountjoy, 1980; Wierzbicki et al., 2006), and hydrothermal dolomitization model (Hardie, 1991; Davies and Smith Jr, 2006), but most of mechanisms of these models are ultimately attributed to replacement, i.e., dolomite is primarily formed by replacing calcite or aragonite with ions such as Mg^{2+} and Fe^{2+} (Land, 1985; Given and Wilkinson, 1987; Budd, 1997; Machel, 2004; Kaczmarek and Thornton, 2017), as these minerals are common metastable precursor for dolomite (Rodriguez-Blanco et al., 2015; Zhang et al., 2021).

Furthermore, researchers have also proposed that dolomite formation under natural conditions does not occur solely through replacement (Huang et al., 2007; McKenzie and Vasconcelos, 2009; He et al., 2010; Petrash et al., 2017; Liu et al., 2019a). For example, highly negative-charged clay minerals such as illite and montmorillonite

* Corresponding author. School of Geosciences, China University of Petroleum (East China), Qingdao, Shandong, 266580, China.
E-mail addresses: xiongzhouhai@126.com (Z. Xiong), caoych@upc.edu.cn (Y. Cao), liangchao0318@163.com (C. Liang).

https://doi.org/10.1016/j.marpetgeo.2024.106694
Received 15 May 2023; Received in revised form 2 January 2024; Accepted 3 January 2024
Available online 7 January 2024

catalyze aid the precipitation of proto-dolomite via electrostatic binding of Mg^{2+} and Ca^{2+} ions and simultaneous desolvation of these strongly hydrated cations (Liu et al., 2019b), which breaks the view on the origin of inorganic precipitation of dolomite. In addition, bacterial action during shallow diagenesis such as sulfate-degrading bacteria (Wright, 1999; Wright and Wacey, 2005; Deng et al., 2010; Bontognali et al., 2012; Krause et al., 2012), methanoic archaea (Roberts et al., 2004; Kenward et al., 2009), fermenting bacteria (Zhang et al., 2015), and various aerobic halophilic bacteria (Rivadeneyra et al., 2006; Sánchez-Román et al., 2008, 2009, 2011; Deng et al., 2010; Balci and Demirel, 2016; Al Disi et al., 2017; Qiu et al., 2017) can also effectively catalyze the nucleation of proto-dolomite and facilitate its subsequent growth.

In recent years, as dolomite has become recognized as one of the vital shale oil reservoirs, including dolomite's intercrystalline pores, dissolution pores, and pores between dolomite crystals and other minerals, have been acknowledged as crucial storage spaces for shale oil in the Jiyang Depression (Zhang et al., 2020; Liang et al., 2022; Xiong et al., 2022). Consequently, many researchers have progressively directed their attention towards the study of the origin of crystalline dolomite in shale (Liu et al., 2019b; Pan et al., 2022; Zhao et al., 2022). Researchers have believed that the origin of ferroan-poor and ferroan-rich dolomite in shale is related to the microbial processes during syngenetic or shallow burial diagenetic stages (Bojanowski, 2014; Teng et al., 2022). Previous studies have shown that ferroan-poor dolomite in the core of ferroan-rich dolomite is formed by biological induction such as bacterial sulfate reduction, exhibiting irregular shapes (Meister et al., 2011; Petrash et al., 2017). Friedman and Murata (1979), suggest that during the early diagenesis of shale, shallowly buried bacterial sulfides degrade, resulting in the formation of light carbon dolomite, while deeply buried microbial fermentation contributes to the development of heavy carbon dolomite.

However, as research has progressed, many researchers have increasingly recognized that the mature stage of shale still facilitates the production of authigenic dolomite, particularly ferrodolomite (Yang et al., 2018; Liu et al., 2019b; Lin et al., 2020). Teng (2018) found that shale intervals with high clay mineral content exhibit a higher abundance of dolomite, particularly when there is an increase in the content of illite and I/S (Illite/Smectite) mixed layers. This indicates that conversion of montmorillonite to illite is beneficial for the formation of dolomite. Previous studies have demonstrated that the release of Fe^{2+} and Mg^{2+} during the illitization of smectite serves as one of the significant sources of materials for the formation of ferrodolomite (Boles and Franks, 1979; Milliken et al., 1994; Yang et al., 2018). Li et al. (2020) also noted that within sand-mud interbedding, ferroan-rich carbonate cement (especially ferrodolomite) between debris particles in silty sand layers, primarily originates from products such as Ca^{2+}, Fe^{2+}, and Mg^{2+} released during the transformation of adjacent clay minerals. Furthermore, the dissolution of early carbonate minerals (Xiong et al., 2022) and mica (Boles and Johnson, 1984; Claeys and Mount, 1991), as well as the thermal evolution of organic matter (Land et al., 1997; Guo et al., 2014), also serve as material sources for the formation of crystalline dolomite in shale. In addition, in regions with well-developed faults, the injection of bottom hydrothermal fluids also plays a significant role in the formation of crystalline dolomite in shale (Jiang et al., 2021; Zhao et al., 2022).

The above investigations suggest that the origin of crystalline dolomite in shale is intricate and involves all stages of diagenesis and sedimentation. Crystalline dolomite with distinct genesis (such as microbial and chemical genesis), distinct stages (such as early and middle diagenesis), and distinct environments (such as the combination of organic matter laminae and clay laminae in mudstone facies, or the combination of organic-rich clay laminae and calcite laminae in limestone facies) exhibit notable differences in composition, texture, and occurrence characteristics (Guo et al., 2014; Al Disi et al., 2017; Yang et al., 2018; Liu et al., 2019b; Xiong et al., 2022). Nevertheless, a thorough examination of the characteristics and origins of these crystalline dolomites in lacustrine shale is still lacking.

Our research takes the fine-grained rocks rich in crystalline dolomite in the Paleogene UMbr 4–LMbr 3 of the Jiyang Depression, as an example to study the characteristics and origin of the crystalline dolomite, with an expectation to improving our understanding of the diagenesis evolution of shale oil reservoirs and the enrichment law of shale oil.

2. Geological setting

The Jiyang Depression (118.69042° E, 37.428975° N), situated in the southeast of the Bohai Bay Basin, is a secondary tectonic unit that extends in an east-west direction (Fig. 1A and B). The Jiyang Depression is bounded by the Luxi uplift in the south, Chengning uplift in the north and west, and Guangrao–Weibei uplift and Qingtuozi uplift in the east (Fig. 1C), with a total area of about 2.62×10^4 km^2 (Wu et al., 2003; Qiu et al., 2006). The Jiyang Depression includes four depressions of Zhanhua, Dongying, Chezhen and Huimin, as well as uplifts such as Chenjiazhuang, Yihezhuang and Linjiafan (Fig. 1C).

Paleogene, Neogene and Quaternary strata were developed in the Jiyang Depression (Fig. 1D). The Paleogene strata from bottom to top are composed of the Kongdian, Shahejie, and Dongying Formations, with a total thickness of about 7 km (Liang et al., 2018a). The Neogene strata from bottom to top are composed of the Guantao and Minghuazhen Formations. The Quaternary stratum is only composed of the Pingyuan Formation. The Shahejie Formation from bottom to top is further divided into four members, i.e., Mbr 4, Mbr 3, Mbr 2 and Mbr 1, of which the UMbr 4–LMbr 3 is a set of carbonate-rich fine-grained sedimentary rocks of semi-deep lacustrine facies (Chen et al., 2016; Liang et al., 2018b; Teng, 2018; Zhang et al., 2016).

These fine-grained rocks primarily consist of clay laminae, calcite laminae, dolomite laminae, silty layer and gypsum layer, with the former three being particularly prevalent. The most common lithofacies include massive mudstone, laminated mudstone, massive limestone, laminated limestone, massive dolostone, and laminated dolostone. The content of dolomite in the UMbr 4–LMbr 3 varies greatly (Fig. 2). In UMbr 4, the dolomite content ranges from 1 to 97%wt, with an average of approximately 13.01%wt (Table 1); In LMbr 3, the dolomite content ranges from 1 to 78%wt, with an average of about 6.17%wt (Table 1). Dolomite in massive and laminated dolostone is primarily composed of micritic dolomite, while crystalline dolomites are widely distributed in mudstone and limestone, but their types and origins are currently lacking comprehensive understanding. Therefore, this study mainly focuses on the study of crystalline dolomite in mudstone and limestone.

3. Samples and methods

The analytical method of this study was firstly based on the observation and sampling of nearly 1100 m of core columns from four key exploration wells (i.e., NY1, FY1, LY1 and L69) (Fig. 2), selecting approximately 300 samples with a spacing of about 3–4 m for thin-section observation, whole rock and clay mineral composition X-ray diffraction, vitrinite reflectance, and total organic carbon content analyses. Based on the comprehensive analysis of these initial test results and combined with the characteristics of crystalline dolomite, this study selected typical samples for further analysis, including FESEM-CL, LA-ICP-MS, micro-area carbon and oxygen isotopes, in situ micro-area strontium isotopes, and electron probe, X-ray fluorescence (XRF), and CL.

FESEM-CL analysis, with a total of 8 samples, was completed at the China University of Petroleum (East China) Key Laboratory of Deep Oil and Gas, carried out by a combination of field emission scanning electron microscopy (FESEM) and cathodoluminescence (CL) system.

LA-ICP-MS analysis, involving a total of 5 thin slice samples of degreased oil, was conducted at the State Key Laboratory of Deposit

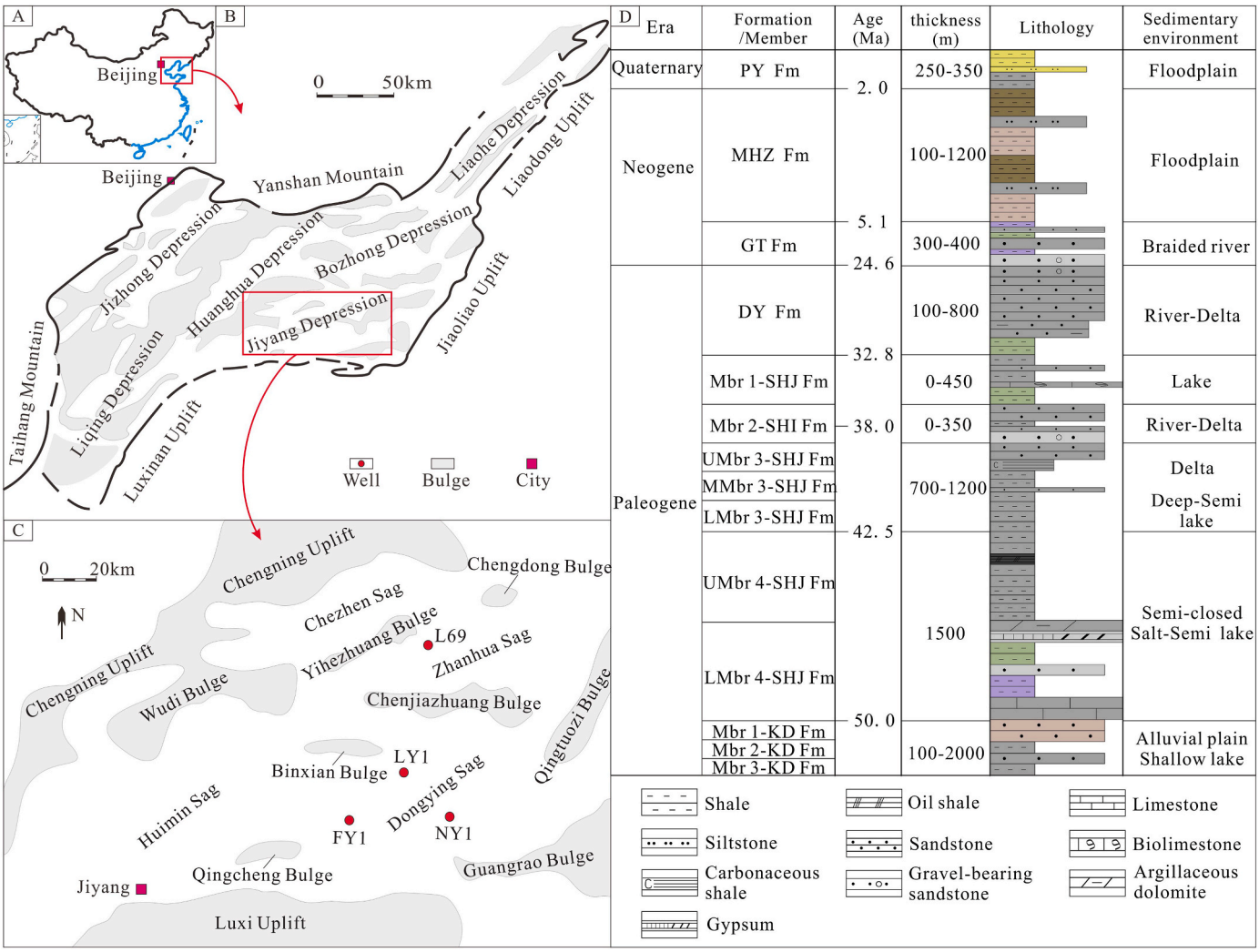

Fig. 1. Structural and stratigraphic characteristics of the study area.
A. China; B. Bohai Bay Basin; C. Jiyang Depression; D. Stratum in the study area. PY Fm—Pingyuan Formation; MHZ Fm—Minghuazhen Formation; Guantao Fm—Guantao Formation; Mbr 1-SHJ Fm—first member of the Shahejie Formation; Mbr 2-SHJ Fm—second member of the Shahejie Formation; UMbr 3-SHJ Fm—upper third member of the Shahejie Formation; MMbr 3-SHJ Fm—middle third member of the Shahejie Formation; LMbr 3-SHJ Fm—lower third member of the Shahejie Formation; Mbr 1-KD Fm—first member of the Kongdian Formation; Mbr 2-KD Fm—second member of the Kongdian Formation; Mbr 3-KD Fm—third member of the Kongdian Formation.

Geochemistry, Institute of Geochemistry, Chinese Academy of Sciences. The analysis employed a combination of laser ablation system (GeoLasPro 193 nm ArF (Argon Fluoride) excimer laser) and ICP-MS instrument (Agilent 7900). During the laser ablation process, helium gas served as the carrier gas, argon gas functioned as the compensation gas, and a small amount of nitrogen gas was added to enhance sensitivity. These gases were mixed through a T-shaped joint before entering the ICP. The laser operated at a frequency of 7 Hz, an energy density of 4–5 J/cm^2, and a beam spot size of 32 μm. Prior to testing, the ICP-MS performance was optimized using Standard Reference Material (SRM) 610 to achieve optimal sensitivity and ionization efficiency (U/Th ≈ 1), minimize oxide yield (ThO/Th < 0.3%), and maintain a low background level. Each collection cycle consisted of approximately 20 s of blank signal followed by 50 s of sample signal. For every 10–15 samples, NIST SRM 610 (National Institute of Standards and Technology Standard Reference Material) was analyzed twice, NIST SRM 612 was analyzed once, and after the test points, NIST SRM 612 was analyzed once again followed by 2 analyses of NIST SRM 610 (i.e., 2 NIST SRM 610 + 1 NIST SRM 612 + 10–15 test points+1 NIST SRM 612 + 2 NIST SRM 610). Sensitivity shift correction was performed using NIST 610 for analysis, while NIST 612 served as the external standard, and calcium (Ca) was used as the internal standard to correct the content of other elements. During data detection, carbonate powder compression MACS-3 (Multi-Analyte Control Set) was employed to monitor data quality. The analysis aimed for an accuracy of most elements in the results better than 10%. Recommended values for element content in calibration materials and quality control samples were based on the GeoReM database (http://georem.mpch-mainz.gwdg.de/). Data processing was conducted off-line using the ICPMSDataCal software.

Micro-area carbon and oxygen isotope analysis, involving a total of 12 samples rich in crystalline dolomites, was conducted at the Key Laboratory of Deep Oil and Gas, China University of Petroleum (East China). The samples were obtained via microdrilling under a microscope, and analyzed using an instrument of Finnigan Mass Analyzer Technology (MAT) 253. The powder samples were reacted in anhydrous phosphoric acid in sealed tubes at a constant temperature of 72 °C for 2 h. The collected CO_2 was used for isotope analysis by the stable isotope ratio mass spectrometry (IRMS), and the ions with mass fractions of 44, 45 and 46 were collected by three receivers respectively. A phosphoric acid fractionation factor of 1.00986 for dolomites (Rosenbaum and Sheppard, 1986) was adopted to calculate the isotopic values. Results are expressed in the usual δ notation in ‰ relative to V-PDB (Vienna-Pee

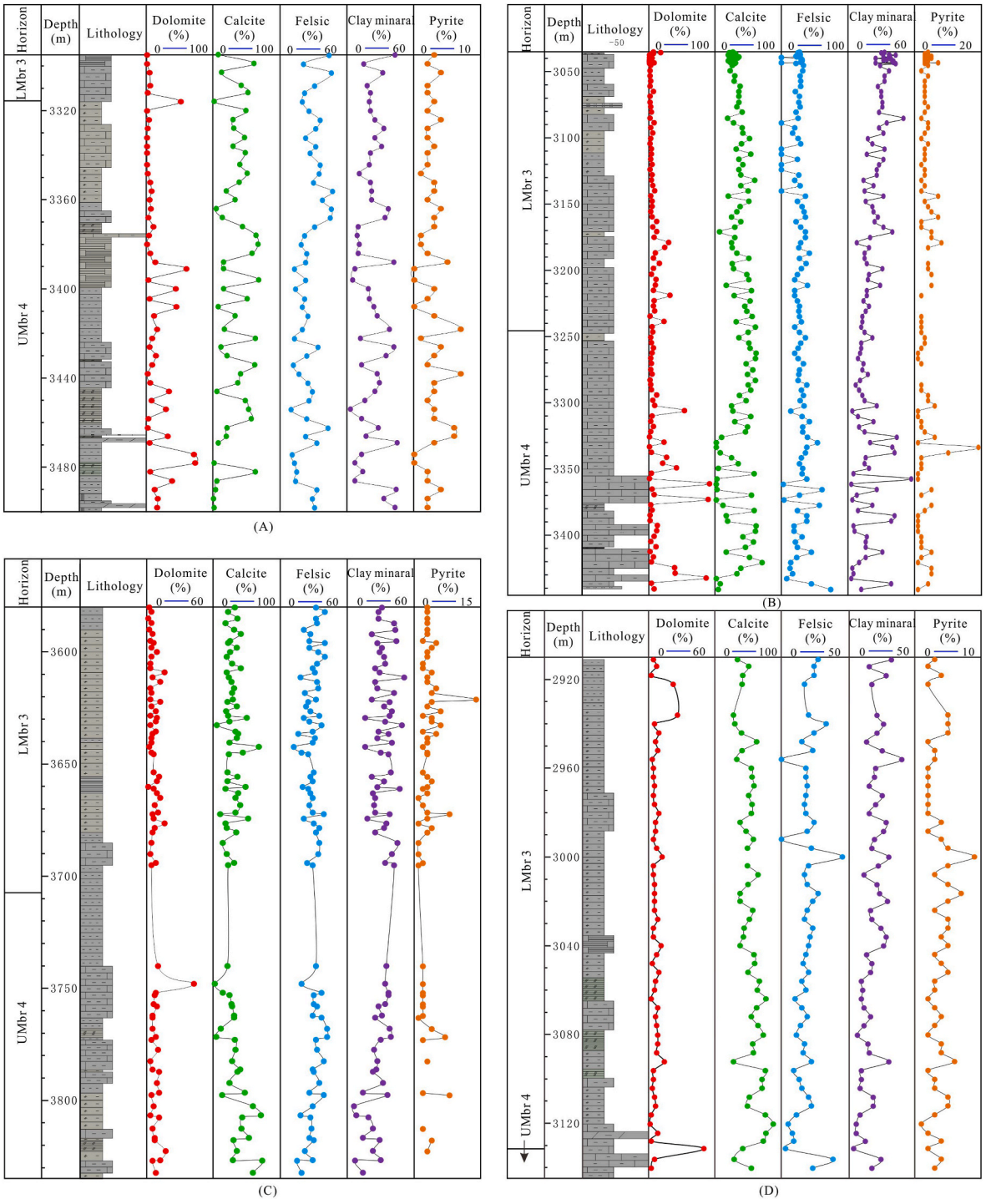

Fig. 2. Distribution characteristics of main mineral components in wells NY1, FY1, LY1, and L69.
A. Distribution characteristics of main mineral components in well NY1; B. Distribution characteristics of main mineral components in well FY1; C. Distribution characteristics of main mineral components in well LY1; D. Distribution characteristics of main mineral components in well L69.

Dee Belemnite) standard for both $\delta^{13}C$ and $\delta^{18}O$. The data is calibrated using a set of internationally recognized reference standards NBS-18 (National Bureau of Standards 18) and IAEA-603 (International Atomic Energy Agency 603), and the standard deviations of $\delta^{13}C$ and $\delta^{18}O$ for the NBS-18 are 0.035‰ and 0.1‰, while 0.01‰ and 0.04‰ for the IAEA-603, respectively. The precision and accuracy of the isotopic measurements are estimated to be better than 0.1‰.

Micro-area Sr isotope analysis, with a total of 6 thin slice samples of degreased oil, was conducted on a Nu Plasma III MC-ICP-MS (Nu Instruments) that was attached to a Resolution-155 ArF193-nm laser ablation system (Australian Scientific Instruments) at State Key laboratory of Ore Deposit Geochemistry, Institute of Geochemistry, Chinese Academy of Sciences. Dolomite was ablated in a mixture of helium (350 ml/min) and nitrogen (2 ml/min) atmosphere using the following parameters: 30 s baseline time, 40 s ablation time, 64 μm spot size, 6 Hz repetition rate and 4 J/cm^2 energy density. The analytical and interference correction protocol follows the method described in Ramos et al. (2004) and was fully addressed in Gao and Zhou (2013). Two in-house

Table 1
Mineral characteristics of fine-grained rocks in the UMbr 4–LMbr 3 of the Jiyang Depression.

Interval	Statistical type	Carbonate minerals (%wt)	Clay minerals (% wt)	Quartz (%wt)	K-feldspar (%wt)	Plagioclase (%wt)	Calcite (%wt)	Dolomite (%wt)	Gypsum (%wt)	Pyrite (%wt)	Siderite (%wt)
LMbr 3	Range	4–94	1–62	3–57	1–5	1–19	1–88	1–78	/	1–16	1–7
	Average	50.27	22.06	21.35	1.21	2.64	44.22	6.17	/	3.48	1.45
	Standard deviation	15.73	9.28	6.62	0.57	2.02	16.19	6.10	/	1.71	0.85
UMbr 4	Range	1–97	2–59	1–60	1–5	1–35	1–91	1–97	1–3	1–34	1–17
	Average	48.93	20.08	22.81	1.67	4.70	36.70	13.01	1.43	2.92	1.23
	Standard deviation	20.43	11.75	9.22	0.96	4.61	21.15	17.29	0.78	2.43	0.96

standards consisting of a modern-day coral (MC) every five samples and a Calcite (BC) every ten unknown samples were treated as quality control. The values of Modern Coral (MC) and Calcite (BC) is 0.709172 (Hodell et al., 1990) and 0.707920 respectively.

Electron probe analysis, with a total of 20 samples, was completed at the Key Laboratory of Deep Oil and Gas, China University of Petroleum (East China), and carried out by a system of electron probe X-ray microanalyser (EPMA-8230). Prior to the experiment, the samples were degreased and processed into specialized probe slices. During the experimental process, target points were first selected under scanning electron microscopy, and then the main element content of these points was automatically detected by wave analysis. The acceleration voltage was 15 kV, the detection current was 1.497E-008, and the Probe Dia was 5 μm.

4. Dolomite characteristics

4.1. Petrological characteristics

Crystalline dolomite is widely developed in different lithofacies of fine-grained rocks, such as massive mudstone, organic-rich laminar mudstone, laminar-massive micritic limestone and dolostone (Fig. 3).

The distribution of crystalline dolomite in mudstone is primarily related to the occurrence in fine-grained rocks. The crystalline dolomite in massive mudstone is mostly distributed sporadically (Fig. 3A). The development of crystalline dolomite in laminated mudstone has two forms: one is that the crystalline dolomite crystals are tightly distributed in lamina (Fig. 3B); another is that the crystalline dolomite crystals is distributed at the boundary between organic-rich and silty clay laminae (Fig. 3C).

The development of crystalline dolomite in clayey limestone also exists in two forms: one is developed inside the calcite laminae, mixed

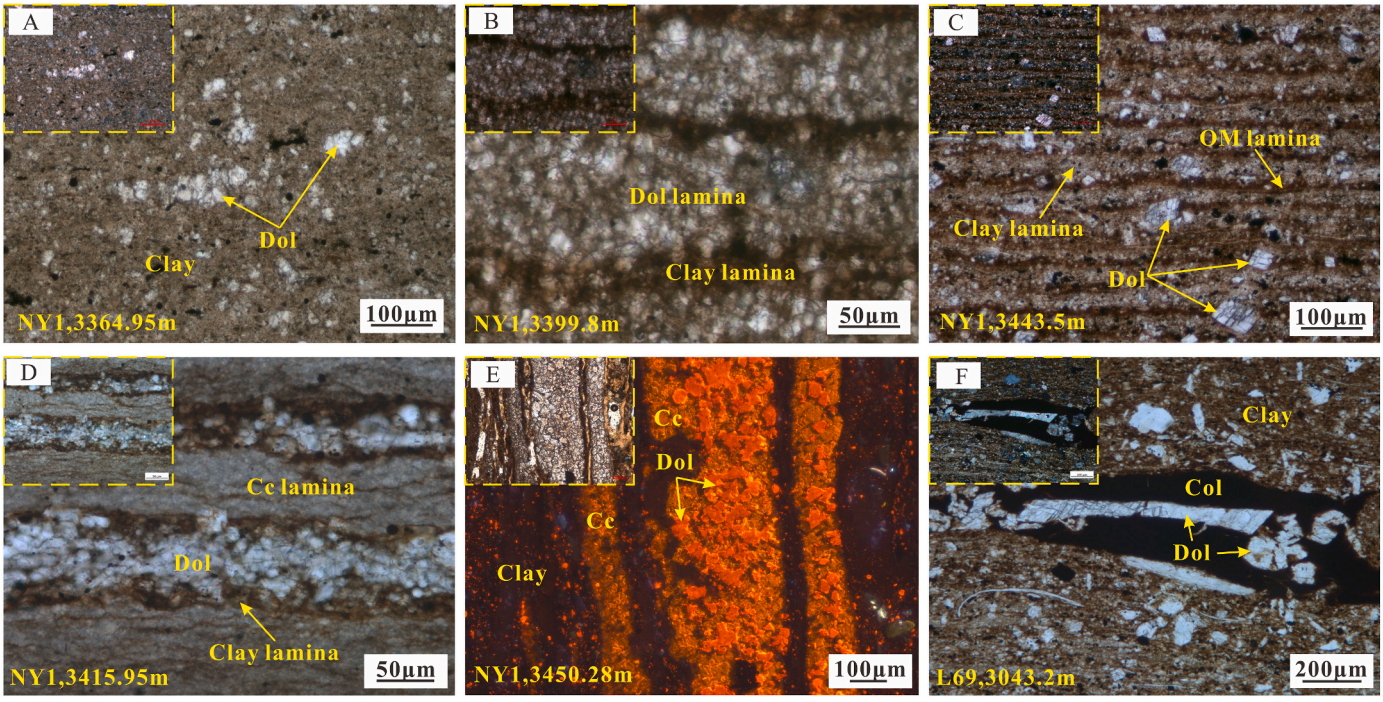

Fig. 3. Characteristics of crystalline dolomite under microscope.
A. The characteristics of crystalline dolomite in massive mudstone, single polarized light, the image in the upper left corner is the corresponding orthogonal light characteristic, NY1, 3364.95 m; B. Layered crystalline dolomite in mudstone, single polarized light, the image in the upper left corner is the corresponding orthogonal light characteristic, NY1, 3399.8 m; C. The characteristics of crystalline dolomite in the laminar interface between the clay lamina and organic matter lamina, single polarized light, the image in the upper left corner is the corresponding orthogonal light characteristic, NY1, 3443.5 m; D. The characteristics of crystalline dolomite in clay laminae of limestone, single polarized light, the image in the upper left corner is the corresponding orthogonal light characteristic, NY1, 3415.95 m; E. The characteristics of crystalline dolomite in granular sparry calcite laminae of limestone, cathodoluminescence, the image in the upper left corner is the corresponding single-polarization characteristic, NY1, 3450.28 m; F. The characteristics of crystalline dolomite in phosphorous binding, single polarized light, the upper left image is the corresponding orthogonal light characteristic, L69, 3043.2 m. Dol—dolomite; OM—organic matter; Cc—calcite; Col—collophanite.

with calcite (Fig. 3E); the other is developed in the laminar boundary between the calcite laminae and the clay laminae. In addition, some are also developed in clay laminae that are coupled with calcite laminae (Fig. 3D);

In dolostone, crystalline dolomite occurs in a variety of types. For instance, crystalline dolomites are distributed in a massive form directly (Fig. 4A), or developed in the fractures of micritic dolostone, with these fractures commonly filled with calcite (Fig. 4B).

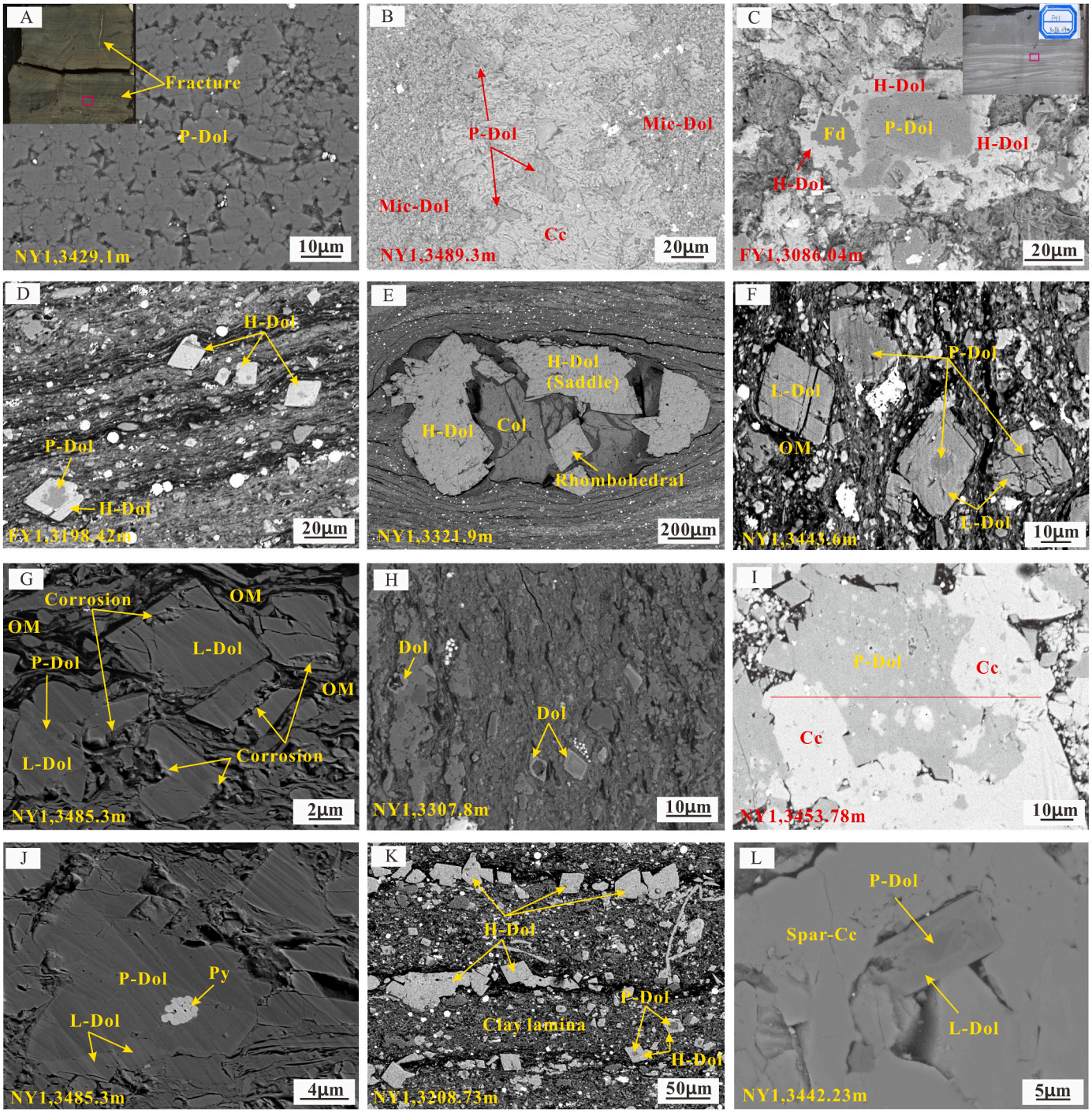

Fig. 4. Characteristics of crystalline dolomite under scanning electron microscope.
A. Characteristics of crystalline dolomite in massive dolostone, backscattered image, the upper left image is the corresponding core characteristic, NY1, 3429.1 m; B. Characteristics of crystalline dolomite in massive dolostone fractures, backscattered image, NY1, 3489.3 m; C. Characteristics of crystalline dolomite in the silt interlayer, backscattered image, the image in the upper right corner is the corresponding core characteristic, FY1, 3086.04 m; D. Characteristics of crystalline dolomite in laminated mudstone, FY1, 3198.42 m; E. Characteristics of crystalline dolomite in phosphorus binding, NY1, 3321.9 m; F. Characteristics of crystalline dolomite in mudstone, NY1, 3443.6 m; G. Dissolution characteristics of crystalline dolomite in mudstone, NY1, 3485.3 m; H. Dissolution characteristics of crystalline dolomite in mudstone, NY1, 3307.8 m; I. Replacement characteristics of crystalline dolomite, NY1, 3453.78 m; J. Framboidal pyrite is wrapped by crystalline dolomite, NY1, 3485.3 m; K. Characteristics of layered crystalline dolomite in laminated mudstone, NY1, 3208.73 m; L. Characteristics of crystalline dolomite in sparry calcite, NY1,3442.23 m. P-Dol—poor dolomite; L-Dol—type I ferroan dolomite; H-Dol—type II ferroan dolomite; Mic Dol—micritic dolomite; Fd—feldspar; Col—collophanite; Cc—calcite; Spar Cc—sparry calcite; Py—pyrite; OM—organic matter.

Furthermore, it is also typical for crystalline dolomite to form in the thin silt interlayer, mostly as cement filler between the detritus grains (Fig. 4C).

4.2. Mineralogical characteristics

The crystal morphology of crystalline dolomite in fine-grained rocks is complex and diverse, such as rhombus, saddle, irregular, etc. (Fig. 4). Generally, the crystalline dolomite is primarily rhombic in organic-rich laminar mudstone (Fig. 4D), and is dominated by irregular shapes in dolostone (Fig. 4A). In addition, the crystalline dolomite in the phosphorus binding has a high euhedral degree, but it also develops in the form of fracture filling (Fig. 3F).

The crystal size of crystalline dolomite in fine-grained rocks varies widely. Statistical analysis has shown that the crystal size of crystalline dolomite varies from 5 to 400 μm, but most are in the range of 10–20 μm (Table 2). Generally, the dolomite crystals involved in phosphorus binding are coarse and take the form of "phenocrysts", with the largest crystals reaching up to 400 μm (Fig. 4E).

The crystalline dolomite in the fine-grained rocks has two crystal types: zoned and unzoned crysals. On the backscattered image, the cores of the zoned dolomites exhibit irregular shapes, often appearing cloudy, circular and spot (Fig. 4D). In addition, there are obvious differences in cathodoluminescence spectra between the core and rim in the zoned crystalline dolomite. As shown in Fig. 5, the cathodoluminescence of the core is obvious and the characteristic peak intensity is strong. Within the wavelength range of 250–800 nm, the main peak is located at 360 nm and the sub-peak band is wide (primarily at 650 nm) (Fig. 5C). The cathodoluminescence of the rim is poor, and the intensity of the characteristic peak is also weak. The main range of the secondary peak shifts to the left, about 620 nm (Fig. 5I).

Crystalline dolomites in fine-grained rocks have been commonly broken, dissolved and replaced. For example, layered crystalline dolomites in laminar mudstone have frequently been characterized by fragmentation and dissolution (Fig. 4F and G), the cores of crystalline dolomites in massive mudstone are often entirely dissolved (Fig. 4H), and ferroan-poor dolomites have also been observed to be replaced by calcite (Fig. 4I). In addition, it was observed that framboidal pyrite was wrapped in dolomitic crystal (Fig. 4J), as well as zoned-dolomitic crystal was wrapped in sparry calcite (Fig. 4L).

4.3. Geochemical characteristics

Statistical analysis shows that the crystalline dolomites in the fine-grained rocks are divided into three categories in terms of FeO content (Fig. 6 and Table 2): the FeO content of the first type is generally less than 1%; the second type is about 5%; the third type is about 16%. In order to facilitate analysis and research, we define crystalline dolomite with FeO content generally less than 1% as ferroan-poor dolomite (FeO $<$ 1%), with FeO content between 1 and 10% as type I ferroan dolomite (FeO $\approx$ 5%), with FeO content more than 10% as type II ferroan dolomite (FeO $\approx$ 16%).

The FeO content of crystalline dolomite in fine-grained rocks is not uniform, but there are noticeable differences in FeO content across different zones. Therefore, based on the petrology, mineralogy and FeO content characteristics of crystalline dolomite, we further divide the crystalline dolomite in fine-grained rocks into five types, as shown in Table 2.

The first type of crystalline dolomite (Dol-1) lacks ring-zonings, is characterized by ferroan-poor dolomite (FeO $<$ 1%), and is primarily distributed in massive dolostone or laminar limestone. As shown in Fig. 5 and Table 3, the CaO content of Dol-1 ranges from 29.213 to 34.630%, the MgO content ranges from 16.652 to 23.181%, and the FeO content ranges from 0.008 to 0.095%, the MnO content ranges from 0.101 to 0.701%, the content of SrO and other major elements is low. The $\delta^{18}O$ of Dol-1 ranges from −0.89 to 0.32‰, and its $\delta^{13}C$ ranges from 3.67 to 4.38‰ (Fig. 7).

The second type of crystalline dolomite (Dol-2) has a ring-zoning, in which the core is characterized by ferroan-poor dolomite (FeO $<$ 1%), the rim is characterized by type I ferroan dolomite (FeO $\approx$ 5%). Dol-2 crystalline dolomites are primarily distributed in laminar mudstone or laminar limestone. As shown in Fig. 5 and Table 3, the average content of CaO in the core of Dol-2 is about 28.300%, the average content of MgO is about 23.768%, the average content of FeO is about 0.608%, the average content of MnO is about is 0.041%, the content of SrO and other elements is low. The average content of CaO in the outer rim of Dol-2 is about 28.657%, the average content of MgO is about 13.422%, the average content of FeO is about 5.405%, the average content of MnO is about 0.586%, the average content of SrO is about 0.087%, and the content of other major elements is low. Compared with the trace elements and rare earth elements in the host rocks, although the content of Dol-2 is generally low, their changing trends are basically the same (Table 4, Table 5 and Fig. 8). The $\delta^{18}O$ of Dol-2 ranges from −3.89 to −3.74‰, and its $\delta^{13}C$ ranges from 5.44 to 5.67‰ (Fig. 7).

The third type of crystalline dolomite (Dol-3) lacks ring-zonings, is primarily characterized by type I ferroan dolomite (FeO $\approx$ 5%), and distributed in laminar mudstone or laminar limestone. As shown in Fig. 5 and Table 3, the CaO content of Dol-3 is 28.260–31.127%, the MgO content is 13.065–21.502%, the FeO content is 3.037–10.298% (about 5% on average), the MnO content is 0.266–1.064%, the content of SrO is 0.081–0.187%, and the content of other major elements is low.

The fourth type of crystalline dolomite (Dol-4) has a ring-zoning, in which the core is characterized by ferroan-poor dolomite (FeO $<$ 1%), the rim is characterized by type II ferroan dolomite (FeO $\approx$ 16%). Dol-4 crystalline dolomites are primarily distributed in organic-rich laminar mudstone. The CaO content of the Dol-4 core is 27.698–32.945%, the MgO content is 17.889–23.327%, the FeO content is 0.225–2.765% (mostly less than 1%), the MnO content is 0.009–0.628%, the SrO content and other major elements are low. The CaO content of the outer rim of the Dol-4 ranges from 25.422 to 28.481%, the MgO content ranges from 8.713 to 10.482%, the FeO content ranges from 15.652 to 17.036% (about 16% on average), and the MnO content ranges from

Table 2
Characteristics of different types of crystalline dolomite in lacustrine shale.

Types	Dol-1	Dol-2	Dol-3	Dol-4	Dol-5
Shape	Irregular, rhombus	Rhombus	Rhombus	Rhombus	Rhombus, saddle
Zoning	No zoning	Zoned	No zoning	Zoned	No zoning
Fe content	Less than 1%	Less than 1% in the core and approximately 5% at the edge	Approximately 5%	Less than 1% in the core and approximately 16% at the edge	Approximately 16%
Size	5–20 μm	10–20 μm	5–20 μm	10–20 μm	10–400 μm
Occurrence	Massive or sporadic within the laminae, filling between the laminae	Laminated, sporadic within the laminae, filling between the laminae	Laminated, sporadic within the laminae, filling between the laminae	Laminated, sporadic within the laminae, filling between the laminae	Sporadic within the laminae, filling between the laminae, associated with phosphorus binding
Lithofacies	Massive dolostone, laminated limestone	Organic-rich laminated mudstone, organic-rich laminated limestone	Organic-rich laminated mudstone, organic-rich laminated limestone	Organic-rich laminated mudstone	Organic-rich laminated mudstone

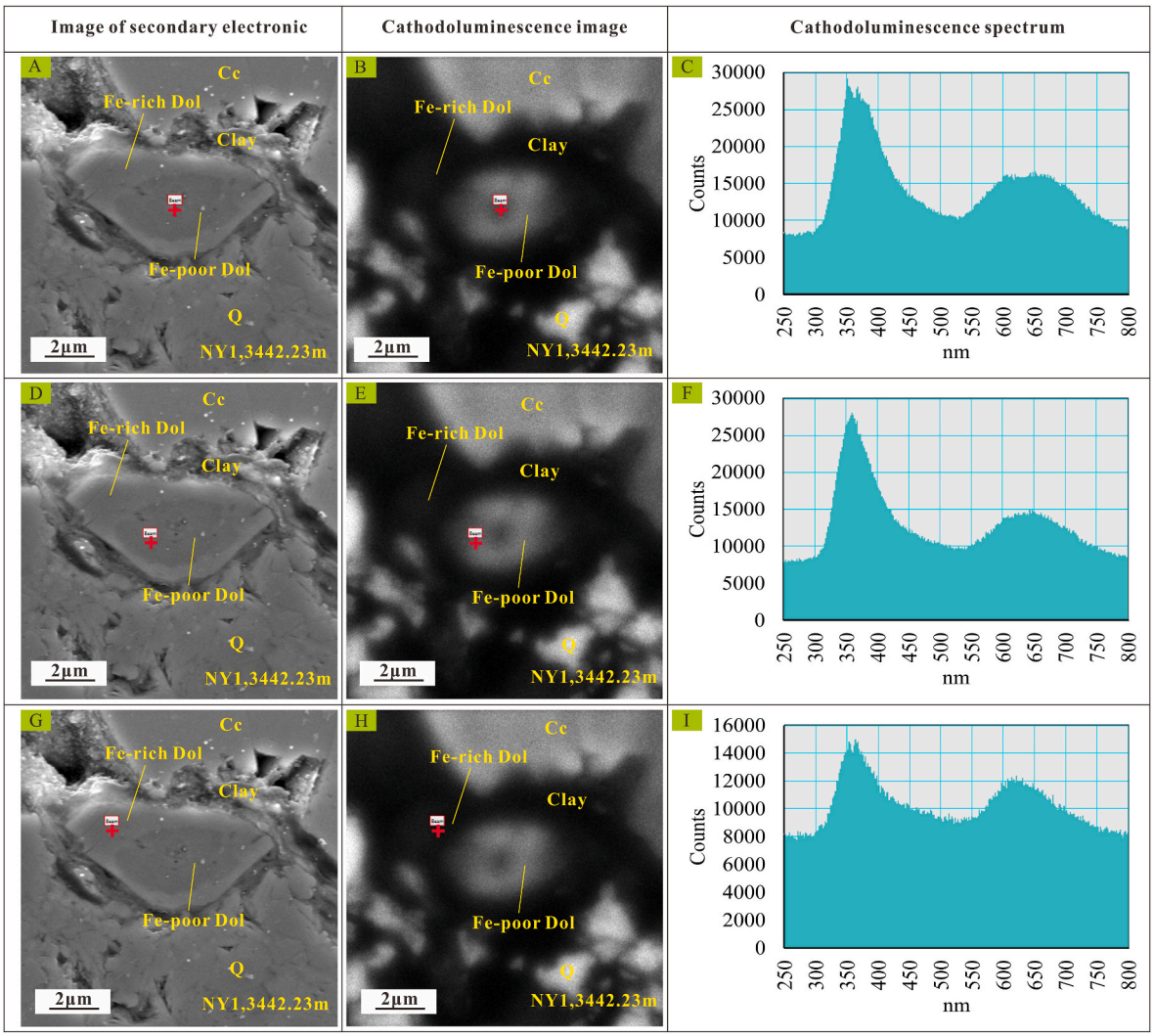

Fig. 5. Cathodoluminescence and spectral characteristics of different positions in crystalline dolomite (NY1, 3442.23 m).
A. Secondary electron image of crystalline dolomite in fine-grained rocks; B. The cathodoluminescence image corresponding to the crystalline dolomite in Figure A; C. Cathodoluminescence spectra corresponding to the red dots in Figure A and B; D. Secondary electron image of crystalline dolomite in fine-grained rocks; E. The cathodoluminescence image corresponding to the crystalline dolomite in Figure D; F. Cathodoluminescence spectra corresponding to the red dots in Figure D and E; G. Secondary electron image of crystalline dolomite in fine-grained rocks; H. The cathodoluminescence image corresponding to the crystalline dolomite in Figure G; I. Cathodoluminescence spectra corresponding to the red dots in Figure G and H. Dol—dolomite; Q—quartz; Cc—calcite.

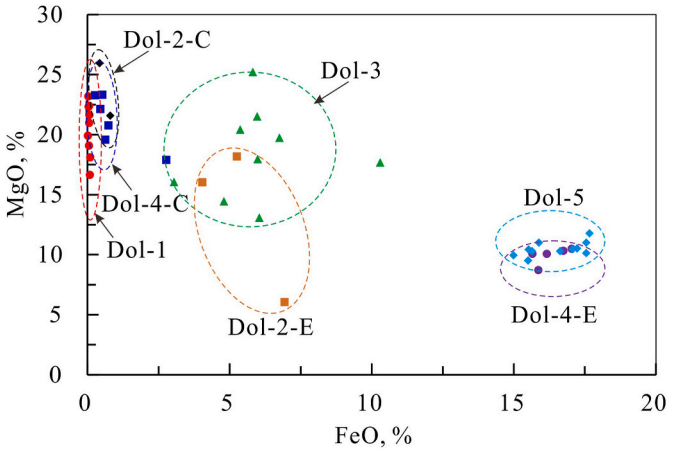

Fig. 6. FeO and MgO content distribution characteristics of different crystalline dolomite.C—the core of crystalline dolomite; E—the edge (rim) of crystalline dolomite.

0.065 to 0.455%. The content of SrO ranges from 0.008 to 0.136%, and the content of other major elements is low.

The fifth type of crystalline dolomite (Dol-5) has no ring-zonings, is characterized by type II ferroan dolomite (FeO ≈ 16%), and primarily distributed in organic-rich laminar mudstone or phosphorus binding. As shown in Fig. 5 and Table 3, the CaO content of the Dol-5 is between 25.354 and 28.450%, the MgO content is between 9.511 and 11.777%, the FeO content is between 14.986 and 17.662% (about 16% on average), and the MnO content is between 0.058 and 0.592%, the SrO content is between 0 and 0.116%, and the content of other major elements is low. As for Dol-5 in phosphorus binding, in addition to Ca, Mg, Fe, Mn, the enrichment degree of Eu and Tb is also relatively high, especially Tb has an abnormally high value (Fig. 9). The Ca content of the Dol-5 is roughly the same as that of phosphorus binding, but phosphorus binding is more enriched in P, Sr, and Ce elements (Fig. 9). Compared with the host rocks, although some rare earth elements and trace elements in Dol-5 crystalline dolomite are abnormal, the overall change trend is basically the same (Table 4, Table 5 and Fig. 8). In addition, the value of $^{87}Sr/^{86}Sr$ in the Dol-5 is between 0.7108 and 0.7111, which is basically indistinguishable from micritic dolomite

Table 3
Major element characteristics in different types of crystalline dolomite based on electron probe.

Number	Type	Total/Core/Edge	Size/μm	Na_2O/%	Al_2O_3/%	SiO_2/%	MgO/%	SrO/%	CaO/%	BaO/%	P_2O_5/%	K_2O/%	FeO/%	MnO/%
NY1_3453.78-2-1	Dol-1	T	20	0.027	0.092	/	19.079	0.008	29.213	0.045	0.061	0.002	0.046	0.109
NY1_3453.78-2-4	Dol-1	T	15	0.017	0.106	/	21.644	0.024	31.246	/	/	0.034	0.063	0.136
NY1_3453.78-2-5	Dol-1	T	15	0.006	0.131	/	22.410	0.098	29.836	/	0.053	0.024	0.053	0.101
NY1_3450.28-2-6	Dol-1	T	10	0.053	0.186	/	18.111	0.024	31.139	0.013	0.012	0.033	0.095	0.239
NY1_3450.28-3-1	Dol-1	T	20	0.039	0.130	/	16.652	0.104	33.520	0.011	/	0.052	0.078	0.196
NY1_3450.28-4-1	Dol-1	T	10	0.023	0.094	/	20.972	0.008	34.630	0.088	0.044	0.015	0.055	0.124
NY1_3450.28-5-1	Dol-1	T	10	0.029	0.071	/	22.318	/	30.817	/	0.057	0.001	0.037	0.324
NY1_3450.28-5-2	Dol-1	T	10	0.036	0.707	3.880	23.181	/	30.814	0.040	0.012	0.070	0.023	0.163
NY1_3451.85-1-3	Dol-1	T	20	0.004	0.058	/	19.904	0.049	29.742	0.053	/	0.023	0.008	0.701
NY1_3485.3-3-1	Dol-2	C	20	/	0.261	0.367	25.955	/	27.695	/	0.012	0.041	0.419	0.020
NY1_3443.6-2-1	Dol-2	C	10	0.049	0.206	/	21.581	/	28.905	0.077	0.025	0.028	0.797	0.062
NY1_3485.3-3-2	Dol-2	E	20	0.034	0.536	0.721	6.050	/	27.134	0.116	0.266	0.074	6.930	0.553
NY1_3485.3-3-3	Dol-2	E	20	0.121	0.624	3.330	16.038	0.024	29.805	0.094	0.094	0.064	4.033	0.405
NY1_3443.6-2-2	Dol-2	E	10	0.023	0.067	/	18.177	0.236	29.031	0.063	/	0.035	5.251	0.800
NY1_3485.3-1-1	Dol-3	T	8	0.069	0.437	0.668	14.434	0.127	30.940	/	0.108	0.087	4.796	0.309
NY1_3485.3-1-3	Dol-3	T	5	0.094	0.958	1.571	13.065	0.087	28.260	/	0.120	0.157	6.041	0.266
NY1_3485.3-1-4	Dol-3	T	10	0.141	1.205	0.740	16.041	0.206	29.917	0.067	0.068	0.107	3.037	0.345
NY1_3485.3-1-5	Dol-3	T	8	0.185	0.745	0.870	17.663	0.080	30.950	0.063	0.497	0.096	10.298	0.686
NY1_3485.3-2-1	Dol-3	T	15	0.087	0.446	0.180	21.502	0.309	31.127	0.044	0.077	0.045	5.966	0.490
NY1_3443.6-1-1	Dol-3	T	8	0.084	0.811	1.238	17.962	0.081	27.646	0.010	0.029	0.160	5.984	0.909
NY1_3443.6-1-3	Dol-3	T	15	0.031	0.077	/	20.410	0.187	30.315	/	0.033	0.021	5.371	0.944
NY1_3443.6-1-4	Dol-3	T	15	0.023	0.083	/	19.723	0.114	29.361	0.031	/	0.021	6.751	1.035
NY1_3443.6-1-5	Dol-3	T	15	0.050	0.051	/	25.206	0.132	28.769	0.041	/	0.009	5.818	1.064
FY1_3198.42-2-1	Dol-4	C	10	0.019	0.021	/	22.132	/	27.698	0.093	/	0.026	0.449	0.042
FY1_3198.42-4-1	Dol-4	C	10	0.084	0.333	0.711	17.889	0.424	30.132	/	0.097	0.059	2.765	0.628
FY1_3198.42-5-1	Dol-4	C	10	0.009	0.019	/	23.271	/	31.383	/	/	0.025	0.255	0.009
FY1_3198.42-8-1	Dol-4	C	10	0.010	0.024	/	20.760	/	28.126	0.045	/	0.038	0.733	0.053
FY1_3208.73-4-1	Dol-4	C	25	0.014	0.038	0.168	23.327	/	29.931	/	/	0.033	0.516	0.024
FY1_3208.73-4-6	Dol-4	C	20	0.084	/	0.107	19.574	0.008	32.945	0.090	0.133	0.030	0.621	0.505
FY1_3198.42-2-2	Dol-4	E	10	0.039	0.055	/	10.069	0.016	25.422	/	0.008	0.045	16.158	0.065
FY1_3198.42-5-2	Dol-4	E	10	0.028	0.040	/	8.713	0.095	28.481	/	/	0.045	15.863	0.215
FY1_3198.42-8-2	Dol-4	E	10	0.007	0.073	0.027	10.315	0.008	25.506	0.023	0.036	0.042	16.743	0.247
FY1_3208.73-4-2	Dol-4	E	25	0.025	0.005	/	10.064	0.136	26.134	0.050	0.004	0.039	15.652	0.260
FY1_3208.73-4-5	Dol-4	E	20	/	0.005	/	10.482	0.120	27.474	/	0.012	0.035	17.036	0.455
FY1_3198.42-3-1	Dol-5	T	8	0.052	0.102	0.693	9.947	0.079	25.532	0.043	0.016	0.057	14.986	0.282
FY1_3198.42-5-4	Dol-5	T	15	0.025	0.014	/	10.452	/	27.186	0.003	/	0.036	17.065	0.401

(*continued on next page*)

Table 3 (*continued*)

Number	Type	Total/Core/Edge	Size/μm	Na_2O/%	Al_2O_3/%	SiO_2/%	MgO/%	SrO/%	CaO/%	BaO/%	P_2O_5/%	K_2O/%	FeO/%	MnO/%
FY1_3198.42-10-8	Dol-5	T	10	0.035	0.048	/	9.511	0.182	26.881	0.088	0.036	0.029	15.503	0.233
FY1_3208.73-1-2	Dol-5	T	30	0.002	0.012	/	10.515	0.104	27.702	/	0.028	0.028	17.226	0.399
FY1_3208.73-1-3	Dol-5	T	20	0.012	0.014	/	11.777	0.016	25.473	0.106	0.004	0.024	17.662	0.117
FY1_3208.73-1-5	Dol-5	T	20	0.088	0.010	0.057	10.425	0.153	26.029	/	0.052	0.022	15.518	0.369
FY1_3208.73-4-3	Dol-5	T	10	0.014	0.003	/	11.004	0.048	25.354	/	/	0.034	15.883	0.058
FY1_3208.73-6-1	Dol-5	T	10	0.021	0.035	/	10.297	0.087	27.513	0.060	0.032	0.022	15.640	0.247
NY1_3321.9-1-2	Dol-5	T	400	0.057	0.025	/	10.291	/	27.476	/	0.004	/	16.630	0.411
NY1_3321.9-1-3	Dol-5	T	400	0.009	0.049	/	10.130	0.176	28.450	/	/	/	17.549	0.386
NY1_3321.9-1-4	Dol-5	T	400	0.037	0.023	/	10.999	0.008	28.315	0.005	0.016	/	17.547	0.592

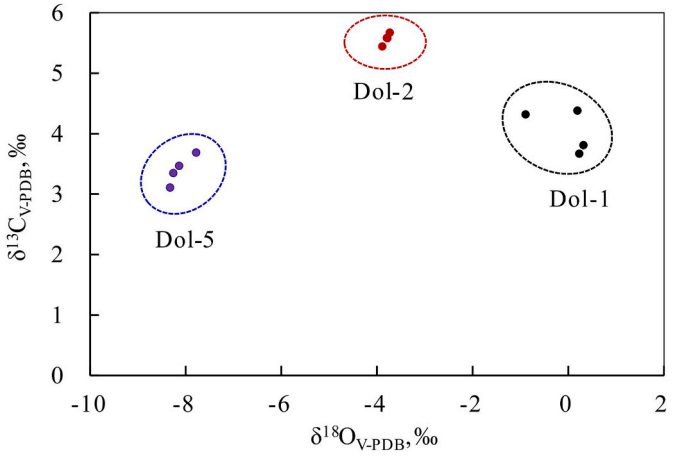

Fig. 7. Micro-area carbon and oxygen isotopic characteristics of Dol-1, Dol-2 and Dol-5 crystalline dolomite.

(Fig. 10). The $\delta^{18}O$ of Dol-5 ranges from −8.33 to −7.78‰, and its $\delta^{13}C$ ranges from 3.11 to 53.69‰ (Fig. 7).

5. Origin analysis

5.1. Dol-1

The formation mechanism of Dol-1 crystalline dolomite is different between mudstone and carbonate rocks. Dol-1 in mudstone is primarily formed by microbial action, while in carbonate rocks is primarily formed by recrystallization.

In organic-rich mudstone, Dol-1 crystals are small, often less than 10 μm, with a low degree of euhedral. It can be deduced that ferroan-poor dolomite and framboidal pyrites were essentially generated at the same diagenetic stage based on the phenomena that framboidal pyrites are associated with or enveloped in the ferroan-poor dolomite (Fig. 4J). It is well known that framboidal pyrite has been considered as the product of microbial action in early diagenetic stage (Taylor et al., 2000; Yang et al., 2018). Therefore, Dol-1 crystalline dolomites are related to microbial action during the early diagenetic stage. Studies have shown that biological action promotes the formation of dolomite (Roberts et al., 2004; Krause et al., 2012; Zhang et al., 2015; Qiu et al., 2017; Al Disi et al., 2017). For example, the hydrated ferric oxides produce a large amount of ferroan-poor carbonate minerals (ferroan-poor dolomite and calcite) and pyrite precipitated by sulfate-reducing bacteria, rather than ferroan-rich carbonate minerals (Curtis, 1978). The ferroan-poor dolomite formed by microbial action is often characterized by Mg-high content (Fig. 12), which may have low stability in later acidic diagenetic fluids and be easily dissolved (Fig. 4G). The carbon and oxygen isotope analysis also showed that the $\delta^{18}O$ ranged from −0.89 to 0.32‰, and the $\delta^{13}C$ ranged from 3.67 to 4.38‰ (Fig. 7). Selecting the $\delta^{18}O_{smow\text{-}water}$ to be 0.25‰ (Han et al., 2012; Yang et al., 2018), and the calculation formula of carbonate cement precipitation temperature proposed by O'Neil (Equations (1) and (2)) (Carothers et al., 1988; O'Neil et al., 1969; Xiao et al., 2021), the precipitation temperature of Dol-1 crystalline dolomite in mudstone is between 45.7 and 52 °C, further indicating that ferroan-poor dolomite was primarily formed in the early diagenetic stage A, which has also been confirmed in previous studies (Wright and Wacey, 2005; Bontognali et al., 2012; Krause et al., 2012; Qiao et al., 2021; Bai et al., 2022; Pan et al., 2022).

$$1000\ ln\ a_{Dolomite-water} = 3.2 \times \frac{10^6}{T^2} - 1.5 \quad (1)$$

$$\alpha_{Dolomite-water} = \left(1 + \frac{\delta^{18}O_{Dolomite}}{1000}\right) \Big/ \left(1 + \frac{\delta^{18}O_{smow-water}}{1000}\right) \quad (2)$$

wherein, $\delta^{18}O$ is the measured oxygen isotope value of dolomite, PDB standard; T is the precipitation temperature of dolomite, °C.

Additionally, it was frequently shown that the early-stage Dol-1 was de-dolomitized and predominantly metasomatized by the later sparry calcite (Fig. 4I). Fe, Na, and K content remained mostly unchanged during the replacement, however Sr and Ca content rose while Mn and Mg content dropped (Fig. 11). The formation of these sparry calcites during the middle diagenetic stage, as explained by Xiong et al. (2022), further suggests that Dol-1 was initially formed during the early diagenetic stage and subsequently underwent replacement by calcite due to changes in the later diagenetic environment.

Recrystallization is a major role in the formation of Dol-1 crystalline dolomite in carbonate rocks. Micritic dolostone has a lot of vertical fractures filled with calcite, as seen in Fig. 3B. Due to the occurrence of crystalline dolomites in proximity to fractures (Fig. 4B), displaying a composition similar to the surrounding micritic dolomite, Dol-1 is believed to have formed as a result of the recrystallization of micritic dolomite during fluid activity after fracture development. According to earlier research (Liang et al., 2018a; Xiong et al., 2022), the calcite filling these fractures is primarily formed in the middle diagenetic stage, further supporting the idea that the crystalline dolomites close to the fractures are formed by the recrystallization of micritic dolomite under the influence of fluids rich in organic acids. In addition, large amounts of vertical fractures are developed in the interior or bottom of the layer

Table 4
Characteristics of rare earth elements in different types of crystalline dolomite and corresponding host rock based on LA-ICP-MS.

Number	Type	La/ppm	Ce/ppm	Pr/ppm	Nd/ppm	Sm/ppm	Eu/ppm	Gd/ppm	Tb/ppm	Dy/ppm	Ho/ppm	Er/ppm	Tm/ppm	Yb/ppm	Lu/ppm
NY1_3441.6-1	Dol-2	9.1802	16.3597	1.6610	6.3174	0.9889	0.2289	0.7640	0.1404	1.0441	0.2149	0.7165	0.0992	0.9146	0.1211
NY1_3441.6-2		7.9644	15.0309	1.6986	6.1619	1.3884	0.2251	0.9174	0.1739	1.1591	0.2242	0.7695	0.1142	0.8516	0.1300
NY1_3441.6-3		13.6940	30.2868	3.5062	14.5225	2.7008	0.5965	2.4066	0.3223	1.8753	0.3637	1.0530	0.1524	0.9558	0.1642
NY1_3441.6-4		9.5062	16.6703	1.6813	5.9331	1.0521	0.2295	1.0817	0.1466	1.2921	0.2362	0.8141	0.1276	1.0024	0.1327
NY1_3321.9-1	Dol-5	6.6008	24.7920	3.6761	16.1466	3.1045	0.9999	0.5434	3.2312	3.0703	0.5784	1.4190	0.1696	0.7493	0.1392
NY1_3321.9-2		7.0362	20.2356	2.6940	11.4009	3.0856	0.7716	0.3110	1.8025	1.2220	0.2564	0.4481	0.0609	0.0889	0.0296
NY1_3321.9-3		23.9683	72.7795	9.6204	38.8755	7.8259	2.2603	0.9108	6.4208	5.1735	1.0044	2.4814	0.2526	1.2243	0.1919
NY1_3321.9-4		19.1442	51.6537	6.8402	26.4419	5.7273	1.9814	0.6989	4.2521	3.4104	0.6263	1.2926	0.1437	0.5323	0.0794
NY1_3321.9-5		2.8052	9.0263	1.2752	5.8209	1.0745	0.5160	0.1605	0.8522	0.8504	0.1187	0.3121	0.0480	0.1437	0.0290
NY1_3321.9-6		39.1140	117.9119	15.8623	65.4277	12.0703	2.8085	1.2730	9.0107	7.1800	1.2710	2.7563	0.3295	1.7846	0.2460
NY1_3321.9-7		31.6074	92.4898	12.3166	50.2727	9.3007	2.1174	1.1137	7.6362	6.1164	1.0229	2.8892	0.3434	1.7218	0.1915
NY1_3321.9-8		29.0769	97.8956	14.3382	62.1321	11.6019	2.5509	1.2414	9.0676	6.3474	0.9975	2.2586	0.2142	1.1748	0.1394
NY1_3321.9-9		3.4685	9.7570	1.3261	6.1166	1.4831	0.7202	0.1350	1.1120	1.0213	0.1301	0.3474	0.0296	0.1801	0.0204
NY1_3321.9-10		4.9137	14.2330	1.9013	8.6058	1.4184	0.8721	0.1902	1.4159	1.0758	0.1585	0.3070	0.0276	0.1245	0.0123
NY1_3441.6-5	Dol-2-Clay	30.5400	55.4469	5.7227	21.5963	4.2155	0.8790	3.7131	0.4992	3.9541	0.7464	2.1898	0.1764	2.1050	0.3029
NY1_3441.6-6		29.7636	50.7738	4.9773	18.8662	3.7910	0.8134	3.4461	0.4967	3.1368	0.6537	2.4500	0.3268	2.6089	0.5401
NY1_3441.6-7		26.1349	50.2118	5.0302	17.4674	3.4167	0.7957	3.4407	0.4664	3.4824	0.6529	2.0314	0.2626	1.9839	0.2865
NY1_3441.6-8		29.4898	64.9503	7.7746	30.8171	6.4508	1.3999	5.8726	0.7734	4.6355	1.0245	3.0522	0.3607	2.2095	0.3546
NY1_3441.6-9		26.9718	50.0846	5.8624	23.3141	3.8223	0.8316	4.4780	0.5208	3.6598	0.7090	2.1156	0.2630	1.8256	0.2644
NY1_3321.9-11	Dol-5-Clay	35.7873	68.9165	7.2100	25.1677	3.9673	1.1291	3.4487	0.5669	3.4683	0.7705	1.9189	0.3435	2.3676	0.4049
NY1_3321.9-12		42.2150	82.3056	9.1720	30.7288	5.9859	1.1270	4.5395	0.7331	4.3386	0.8698	2.0230	0.3621	2.1253	0.3059
NY1_3321.9-13		61.8066	119.9265	13.4033	50.3331	9.6208	1.7609	6.1617	0.7769	4.3057	0.8330	1.9811	0.2966	2.1902	0.3161
NY1_3321.9-14		50.6206	86.8908	9.4449	30.9736	4.2536	1.0357	3.4962	0.4735	3.5265	0.7567	2.1849	0.3815	2.2431	0.3285
NY1_3321.9-15		43.5202	77.1324	8.2619	24.6617	4.1792	1.0243	3.9732	0.5464	3.5019	0.8522	2.4330	0.3996	2.4344	0.3771
Average for Dol-2		10.0862	19.5869	2.1368	8.2337	1.5326	0.3200	1.2924	0.1958	1.3427	0.2597	0.8383	0.1233	0.9311	0.1370
Average for Dol-5		16.7735	51.0774	6.9851	29.1241	5.6692	1.5598	0.6578	4.4801	3.5468	0.6164	1.4512	0.1619	0.7724	0.1079
Average for Dol-2-Clay		28.5800	54.2935	5.8734	22.4122	4.3393	0.9439	4.1901	0.5513	3.7737	0.7573	2.3678	0.2779	2.1466	0.3497
Average for Dol-5-Clay		46.7899	87.0344	9.4984	32.3730	5.6014	1.2154	4.3239	0.6194	3.8282	0.8164	2.1082	0.3567	2.2721	0.3465
CI Carbonaceous chondrite		0.2370	0.6130	0.0928	0.4570	0.1480	0.0563	0.1990	0.0361	0.2460	0.0546	0.1600	0.0247	0.1610	0.0246

The data of CI Carbonaceous chondrite derived from McDonough and Suna (1995).

Table 5
Characteristics of trace elements in different types of crystalline dolomite and corresponding host rock based on LA-ICP-MS.

Number	Type	Li/ ppm	Sc/ ppm	V/ppm	Cr/ppm	Co/ ppm	Ni/ppm	Zn/ ppm	Ga/ ppm	As/ ppm	Rb/ ppm	Y/ppm	Zr/ppm	Nb/ ppm	Mo/ ppm	Cd/ ppm	Cs/ ppm	Hf/ ppm	Ta/ ppm	Pb/ ppm	Th/ ppm	U/ ppm
NY1_3441.6-1	Dol-2	14.499	8.251	104.109	28.509	51.986	117.395	12.914	7.289	93.671	24.072	6.217	11.931	1.558	24.073	0.105	1.472	0.345	0.119	89.815	2.331	1.866
NY1_3441.6-2		18.203	8.357	101.833	31.465	4.253	8.756	8.350	7.679	4.058	31.284	6.763	23.635	1.966	2.423	0.062	1.966	0.698	0.128	4.459	3.042	2.498
NY1_3441.6-3		18.179	7.541	92.312	25.740	4.228	6.946	8.688	6.648	3.076	28.019	10.368	19.527	1.374	1.806	0.135	1.829	0.575	0.110	2.825	5.821	3.470
NY1_3441.6-4		14.458	9.498	121.697	33.586	3.822	8.054	7.903	7.336	4.508	27.950	7.297	21.359	1.877	3.258	0.000	1.814	0.620	0.128	5.621	2.586	2.558
NY1_3321.9-1	Dol-5	0.471	7.061	20.602	1.317	0.257	0.000	3.794	1.467	0.176	0.134	18.438	0.142	2.238	0.135	0.237	0.025	0.017	0.007	0.041	0.258	0.054
NY1_3321.9-2		0.844	0.069	4.537	4.570	0.211	0.437	3.084	1.121	0.126	0.337	6.688	0.845	0.000	0.218	0.000	0.052	0.028	0.006	0.132	0.861	0.263
NY1_3321.9-3		0.303	5.800	12.277	2.148	0.210	0.000	5.197	1.015	0.207	0.007	25.119	0.082	0.000	0.140	0.000	0.006	0.000	0.003	0.033	0.453	0.314
NY1_3321.9-4		0.128	0.906	12.372	0.473	0.147	0.000	5.328	0.783	0.000	0.000	17.476	0.136	0.000	0.079	0.090	0.000	0.010	0.000	0.019	0.040	0.095
NY1_3321.9-5		0.153	0.204	10.042	0.501	0.108	0.431	5.157	1.014	0.000	0.037	4.406	0.071	0.005	0.050	0.000	0.000	0.005	0.002	0.014	0.170	0.123
NY1_3321.9-6		0.262	12.796	15.286	0.721	0.154	1.256	5.002	1.325	0.325	0.000	31.431	0.080	0.000	0.118	0.000	0.000	0.001	0.002	0.039	0.852	0.527
NY1_3321.9-7		0.000	11.276	14.717	1.232	0.238	1.242	5.041	1.213	0.029	0.043	28.532	0.118	0.012	0.187	0.088	0.011	0.004	0.002	0.034	0.669	0.391
NY1_3321.9-8		0.215	2.915	5.744	0.581	0.124	0.086	5.053	0.662	0.335	0.023	25.286	0.035	0.000	0.074	0.033	0.000	0.000	0.000	0.007	1.921	0.852
NY1_3321.9-9		0.030	0.082	5.098	0.707	0.165	0.000	5.603	0.529	0.340	0.009	4.490	0.013	0.000	0.041	0.030	0.009	0.000	0.000	0.005	0.025	0.082
NY1_3321.9-10		0.079	0.000	7.399	0.171	0.091	0.842	3.934	0.920	0.014	0.034	4.976	0.082	0.000	0.113	0.053	0.015	0.000	0.002	0.022	0.044	0.259
NY1_3321.9-1		0.471	7.061	20.602	1.317	0.257	0.000	3.794	1.467	0.176	0.134	18.438	0.142	2.238	0.135	0.237	0.025	0.017	0.007	0.041	0.258	0.054
NY1_3441.6-5	Dol-2-Clay	92.058	20.607	277.033	152.500	21.884	40.820	31.235	43.467	7.695	202.425	18.539	117.557	12.541	10.440	0.152	12.315	3.659	0.858	25.914	9.498	6.466
NY1_3441.6-6		89.297	22.638	224.263	123.393	12.005	26.703	24.663	35.924	5.686	185.808	17.870	235.329	14.452	6.584	0.000	14.112	6.069	1.262	14.811	8.595	7.338
NY1_3441.6-7		82.102	14.356	200.974	120.682	31.163	66.549	36.810	35.501	18.137	176.234	20.894	120.466	12.102	16.177	0.240	10.485	3.161	0.770	33.994	8.941	10.848
NY1_3441.6-8		83.141	16.381	233.211	119.837	17.649	37.858	27.579	35.772	10.148	177.259	26.133	135.984	12.967	17.096	0.000	11.678	3.957	0.860	20.268	11.539	15.826
NY1_3441.6-9		77.781	15.797	214.525	110.712	20.454	36.438	29.867	32.028	10.400	165.214	19.182	110.247	13.059	13.540	0.000	10.811	3.266	0.867	31.511	8.519	8.685
NY1_3321.9-11	Dol-5-Clay	65.680	21.142	155.751	103.988	16.581	69.300	23.728	39.471	3.816	148.674	19.724	109.459	11.852	12.533	0.000	9.663	2.952	0.664	19.338	7.318	6.512
NY1_3321.9-12		58.712	20.892	136.542	86.932	14.687	49.832	20.976	39.947	4.934	132.407	21.820	84.431	7.867	9.152	0.000	7.892	2.314	0.533	20.207	8.678	5.827
NY1_3321.9-13		76.802	15.657	212.452	137.381	14.388	46.624	36.818	42.128	4.540	194.772	19.616	125.018	12.714	10.830	0.248	12.531	3.508	0.928	18.930	11.216	7.632
NY1_3321.9-14		73.884	15.281	170.585	123.379	30.850	77.246	25.040	40.284	5.190	160.307	19.114	119.007	12.206	12.081	0.000	10.729	3.175	0.803	26.006	9.231	7.217
NY1_3321.9-15		78.958	18.905	196.393	133.780	14.112	46.998	31.848	42.768	4.121	180.141	21.686	145.833	11.632	9.000	0.458	11.768	4.633	0.796	18.218	8.297	8.955
Average for Dol-2		16.335	8.412	104.988	29.825	16.072	35.288	9.464	7.238	26.328	27.831	7.661	19.113	1.694	7.890	0.075	1.770	0.560	0.121	25.680	3.445	2.598
Average for Dol-5		0.249	4.111	10.808	1.242	0.170	0.429	4.719	1.005	0.155	0.062	16.684	0.160	0.225	0.116	0.053	0.012	0.007	0.002	0.035	0.529	0.296
Average for Dol-2-Clay		84.876	17.956	230.001	125.425	20.631	41.674	30.031	36.539	10.413	181.388	20.524	143.917	13.024	12.767	0.078	11.880	4.022	0.923	25.300	9.418	9.833
Average for Dol-5-Clay		70.807	18.375	174.345	117.092	18.123	58.000	27.682	40.919	4.520	163.260	20.392	116.750	11.254	10.719	0.141	10.517	3.316	0.745	20.540	8.948	7.229
CI Carbonaceous chondrite		1.500	5.920	56.000	2650	500	10500	310	9.200	1.850	2.300	1.570	3.820	0.240	0.900	0.710	0.190	0.103	0.014	2.470	0.029	0.007

The data of CI Carbonaceous chondrite derived from McDonough and Suna (1995).

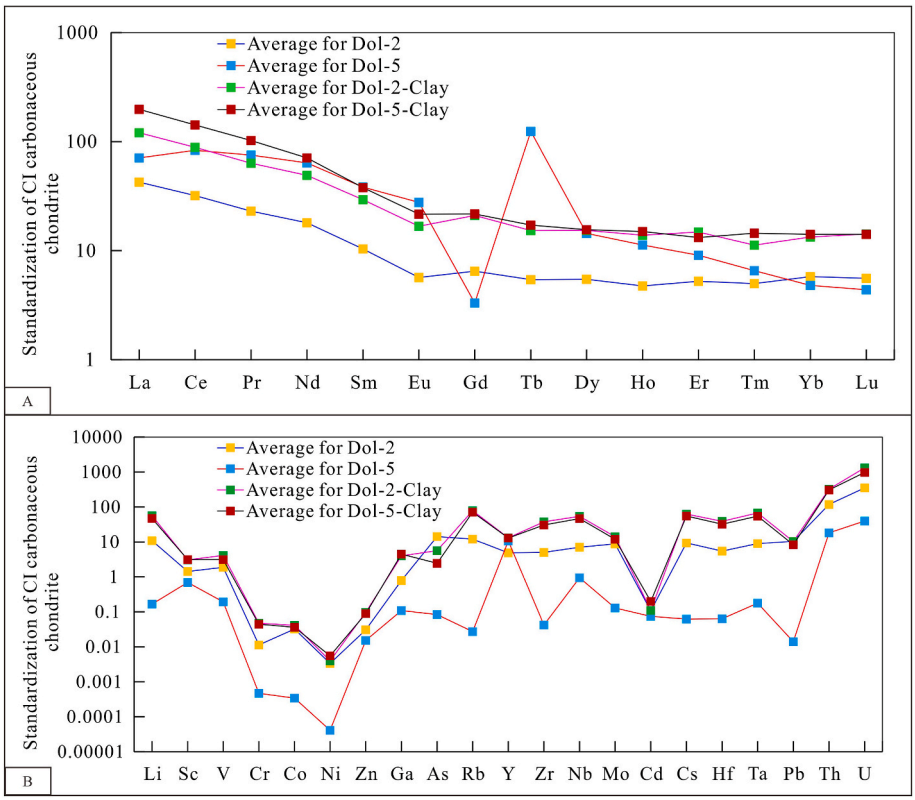

Fig. 8. Distribution characteristics of rare earth and trace elements in crystalline dolomite and its host rock.
A. REE distribution characteristics of Dol-2, Dol-5 and their host rocks; B. Trace element distribution characteristics of Dol-2, Dol-5 and their host rocks.

where laminar or massive crystalline dolomite is developed (Fig. 4A), which also indicates that these crystalline dolomites are formed by recrystallization of early micritic dolomite. Of course, the previous micritic dolomite has a major role in determining the FeO concentration of the crystalline dolomite formed by recrystallization (Liu et al., 2019b; Koeshidayatullah et al., 2020; Zhao et al., 2022).

5.2. Dol-2

Dol-2 crystalline dolomites are primarily developed in organic-rich mudstone. The $\delta^{18}O$ of Dol-2 is between −3.74 and −3.89‰ (Fig. 7), and the $\delta^{18}O_{smow\text{-}water}$ is also selected to be 0.25‰ (Han et al., 2012; Yang et al., 2018), so the corresponding precipitation temperature is between 68.4 and 69.4 °C. Therefore, Dol-2 crystalline dolomites are mainly formed during the early diagenetic stage B (The categorization scheme is widely used in China's oil and gas industry, with Ro ranging from 0.35% to 0.5%, as shown in Fig. 13), when the organic matter has not yet matured in large quantities. According to the crystal texture (Fig. 4F), the rim of Dol-2 crystalline dolomite is rich in Fe and Sr, and poor in Mg, while the core is rich in Mg and poor in Fe and Sr (Fig. 12), and the core is characterized by clouds, circles and spots (Fig. 4), so it is inferred that Dol-2 crystalline dolomite may be formed by replacing ferroan-poor dolomite with type I ferroan dolomite. Furthermore, Dol-2 crystalline dolomites have better euhedral degrees and are typically coarser in crystal size than ferroan-poor dolomites (Fig. 12), demonstrating that Dol-2 crystalline dolomites are not only formed by replacement but also undergo concurrent crystal enlargement caused by the presence of Fe-rich fluid. In fact, during the early diagenetic stage, the source of Fe is divided into two aspects, microbial action (Wright, 1999; Wright and Wacey, 2005; Deng et al., 2010; Bontognali et al., 2012; Krause et al., 2012) and clay mineral transformation (Yang et al., 2018; Liu et al., 2019b). Microbial action such as bacterial sulfide degradation of ferric hydroxide releases a large amount of Fe, which is an important Fe source for ferroan-rich calcite and dolomite in addition to pyrite precipitation (Curtis, 1978; Yang et al., 2018). During the early diagenetic stage B (Fig. 13), when the local temperature was higher than 60 °C, smectite gradually began to transform into the illite/smectite mixed layers (Essene and Peacor, 1995; Potter et al., 2005; Xiong et al., 2022), and releasing large amounts of Ca^{2+}, Fe^{2+}, Mg^{2+} and Na^{+}, as shown in Formula (3). It is also the material source of authigenic calcite, dolomite, quartz, and albite in mudstone (Hower et al., 1976; Lynch et al., 1997; Van De Kamp, 2008; Thyberg et al., 2010; Thyberg and Jahren, 2011; Milliken et al., 2016, 2021; Liang et al., 2018a; Milliken, 2019; Xiong et al., 2022).

$$KNaCa_2Mg_4Fe_4Al_{14}Si_{38}O_{100}(OH)_{20}\bullet 10H_2O + 4.5K^{+} + 8Al^{3+} \rightarrow K_{5.5}Mg_2Fe_{1.5}Al_{22}Si_{35}O_{100}(OH)_{20} + Na^{+} + 2Ca^{2+} + 2.5Fe^{2+} + 2Mg^{2+} + 3Si^{4+} + 10H_2O \quad (3)$$

Additionally, Dol-2 crystalline dolomites in organic-rich laminar mudstone are frequently observed to be dissolved (Fig. 4F), and these acids are primarily released from the thermal evolution of organic matter (Liang et al., 2018a; Xiong et al., 2022), which further suggests that the Dol-2 crystalline dolomites are primarily formed before the thermal evolution of organic matter to generate hydrocarbons, and also indicates that the early-formed ferroan-poor or type I ferroan dolomites are easily dissolved during the organic matter mature stage.

5.3. Dol-3

Dol-3 crystalline dolomites are most frequently found in organic-rich mudstone together with Dol-2 crystalline dolomites (Fig. 4F), and their compositional characteristics are largely consistent with the rim-zoning of Dol-2 (Fig. 6), which indicates that Dol-3 crystalline dolomite are a further evolution of Dol-2 crystalline dolomite and should be formed through the complete replacement of ferroan-poor dolomite with type I ferroan dolomite. Additionally, Dol-3 crystalline dolomites are also

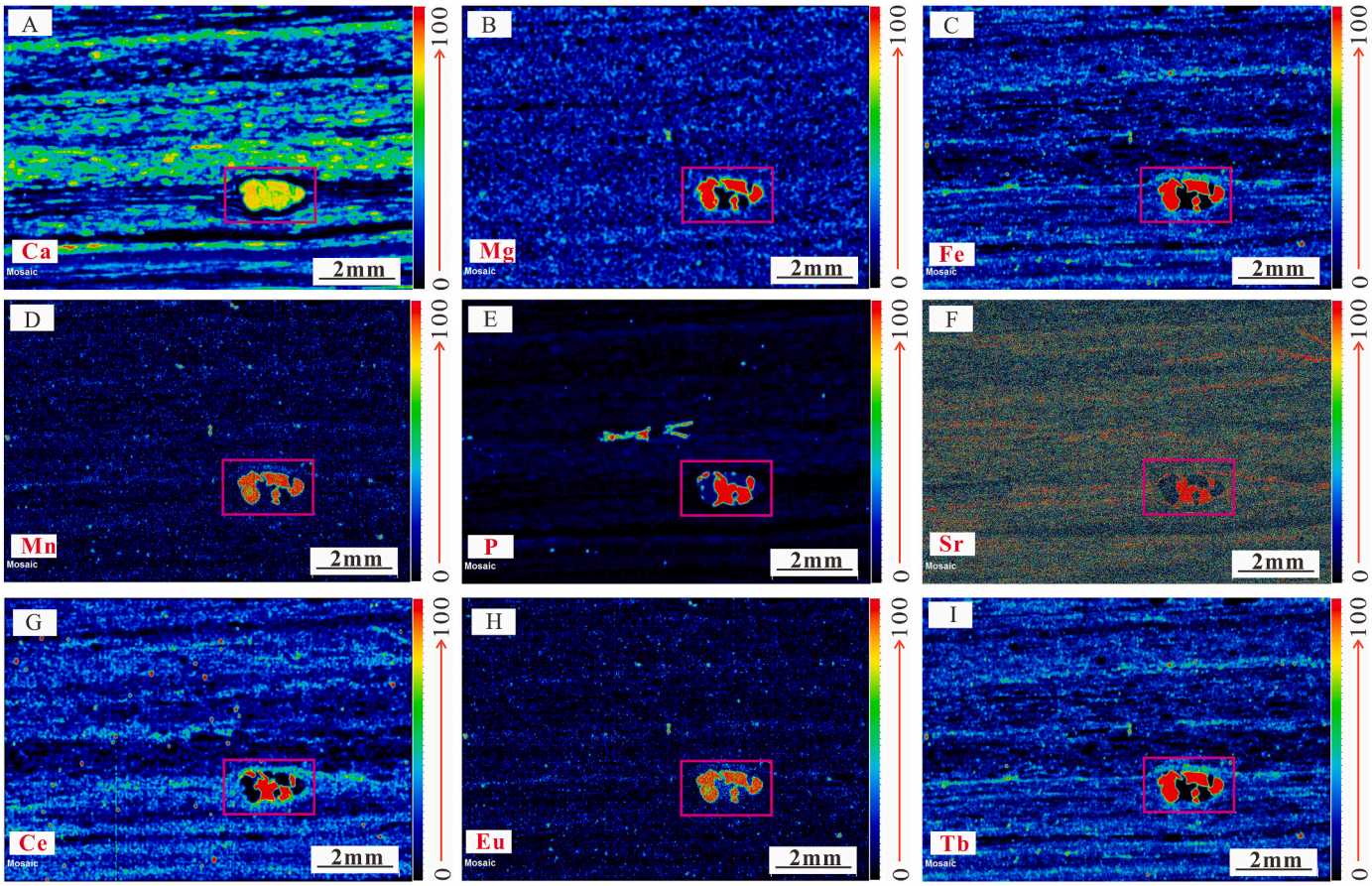

Fig. 9. Elemental distribution characteristics of XRF scanning of Dol-5 crystalline dolomite.
A. Distribution characteristics of Ca content, the red box is the Dol-5 crystalline dolomite in the collophosphate, corresponding to Fig. 3E, NY1, 3321.9 m, the same below; B. Distribution characteristics of Mg content; C. Distribution characteristics of Fe content; D. Distribution characteristics of Mn content; E. Distribution characteristics of P content; F. Distribution Characteristics of Sr Content; G. Distribution Characteristics of Ce Content; H. Distribution Characteristics of Eu Content; I. Distribution characteristics of Tb content.

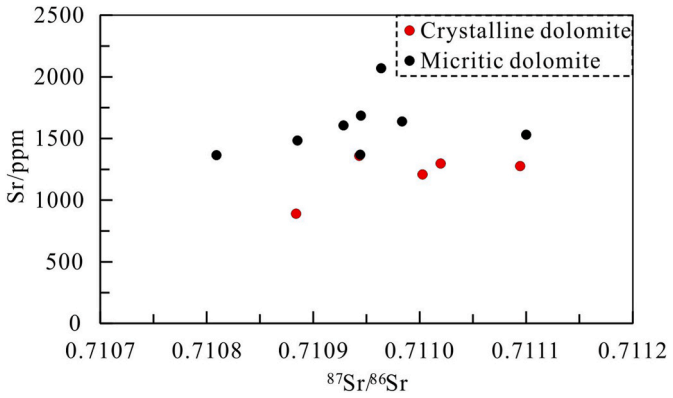

Fig. 10. Sr isotopic characteristics of micritic dolomite and Dol-5 crystalline dolomite.

commonly corroded (Fig. 4G), which also confirms that Dol-3 was formed earlier than the thermal maturity of organic matter, that is, it was mainly formed during the early diagenetic stage. However, the difference from Dol-2 is that Dol-3 crystalline dolomite may also be formed by direct precipitation of diagenetic fluids, driven by the action of microorganisms or clay mineral catalysis. Previous studies have also shown that the action of microorganisms, especially the action of sulfate-reducing bacteria, releases a significant quantity of Fe^{2+}, which leads to the precipitation of ferroan-rich dolomite, accompanied by large amounts of framboidal pyrites (Curtis, 1978; Wright, 1999; Wright and Wacey, 2005; Deng et al., 2010; Bontognali et al., 2012; Krause et al., 2012; Yang et al., 2018).

5.4. Dol-4

Dol-4 crystalline dolomites are primarily developed in organic-rich laminar mudstone, and frequently accompanied with Dol-5 crystalline dolomites (Fig. 4D). The related Dol-5 has an $\delta^{18}O$ range of −7.78 to −8.33‰ with precipitation temperatures of 97–101.5 °C (Fig. 7), indicating that the Dol-4 crystalline dolomite originated during the middle diagenetic stage of the organic matter maturity period. In addition, the authigenic columnar sparry ferroan-rich calcite associated with Dol-4 crystalline dolomite has coarse crystals, which is convenient for inclusion analysis, and the homogenization temperature of brine inclusions is between 90 and 130 °C(Xiong et al., 2022). This also further reveals that the ferroan rim-zoning of Dol-4 was primarily formed during the middle diagenetic stage. From Table 1, it can be seen that the composition of the fine-grained rocks is mostly made up of feldspar, quartz, dolomite, calcite, and clay minerals. When organic matter enters the high-maturity stage, both organic acid yield and clay mineral conversion rate reach their peaks (Lu et al., 2004; Środoń et al., 2006; Milliken, 2019; Xiong et al., 2022). Therefore, the dissolution of early calcite and dolomite (Figs. 4G and 12B) as well as the transformation of clay minerals may potentially serve as sources of Ca, Mg, and Fe for Dol-4.

According to the characteristics of crystal texture, Dol-4 crystalline dolomite is composed of the core characterized by ferroan-poor

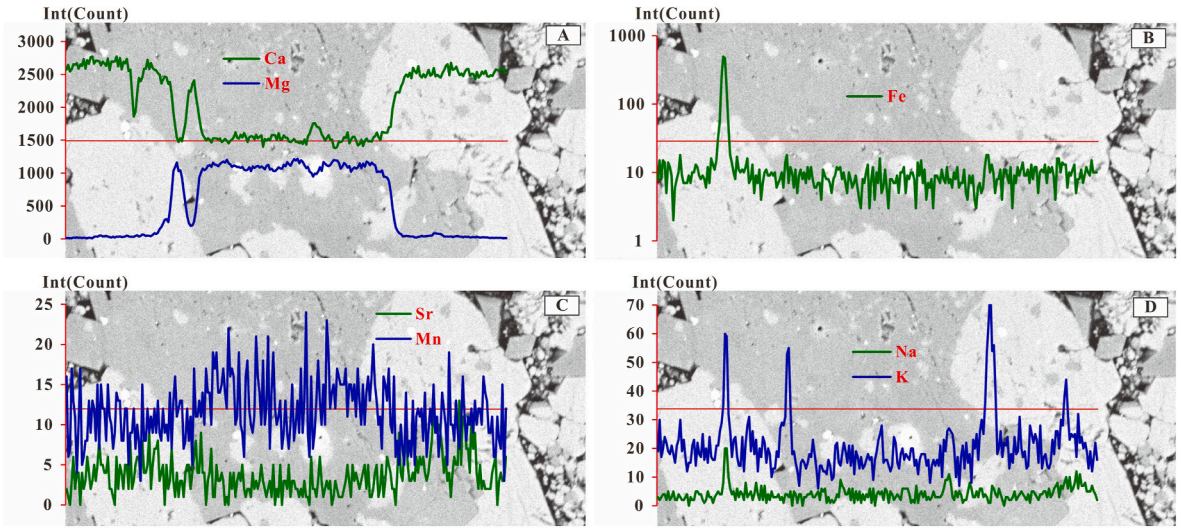

Fig. 11. Element content characteristics of dolomite replaced by calcite.
Note: This figure corresponds to the magnification of the crystalline dolomite in Fig. 4I.

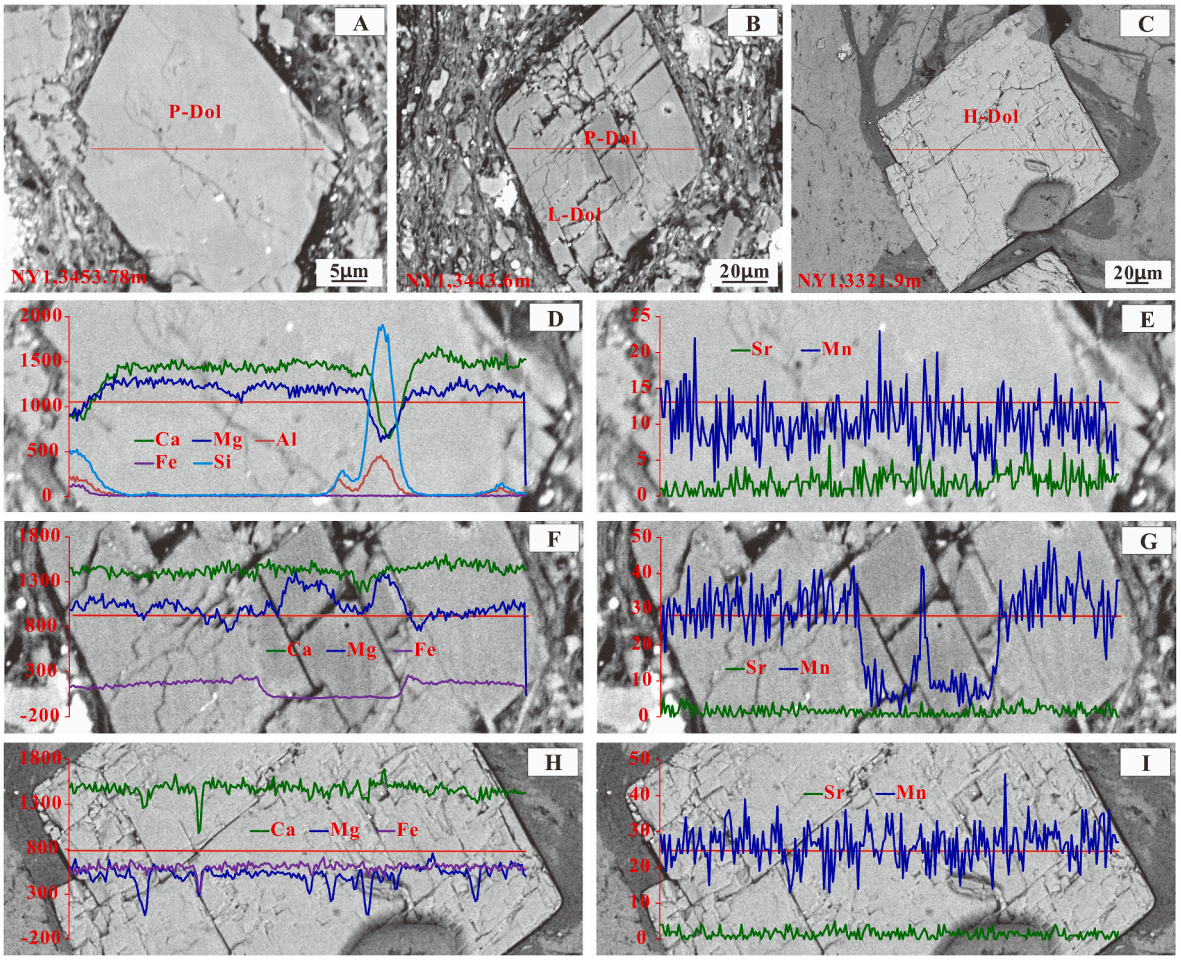

Fig. 12. Characteristics of element content in Dol-2, Dol-3 and Dol-3 dolomites.
A. Dol-1 crystalline dolomite, NY1, 3453.78 m; B. Dol-2 crystalline dolomite, NY1, 3443.6 m; C. Dol-5 crystalline dolomite, NY1, 3321.9 m; D. Characteristics of Ca, Mg, Al, Fe and Si corresponding to the line scan in Figure A, NY1, 3453.78 m; E. Characteristics of Sr and Mn corresponding to the line scan in Figure A, NY1, 3453.78 m; F. Characteristics of Ca, Mg and Fe corresponding to the line scan in Figure B, NY1, 3443.6 m; G. Characteristics of Sr and Mn corresponding to the line scan in Figure B, NY1, 3443.6 m; H. Characteristics of Ca, Mg and Fe corresponding to the line scan in Figure C, NY1, 3321.9 m; I. Characterization of Sr and Mn corresponding to line scan in Figure C, NY1, 3321.9 m. P-Dol—ferroan-poor dolomite; L-Dol—type I ferroan dolomite; H-Dol—type II ferroan dolomite.

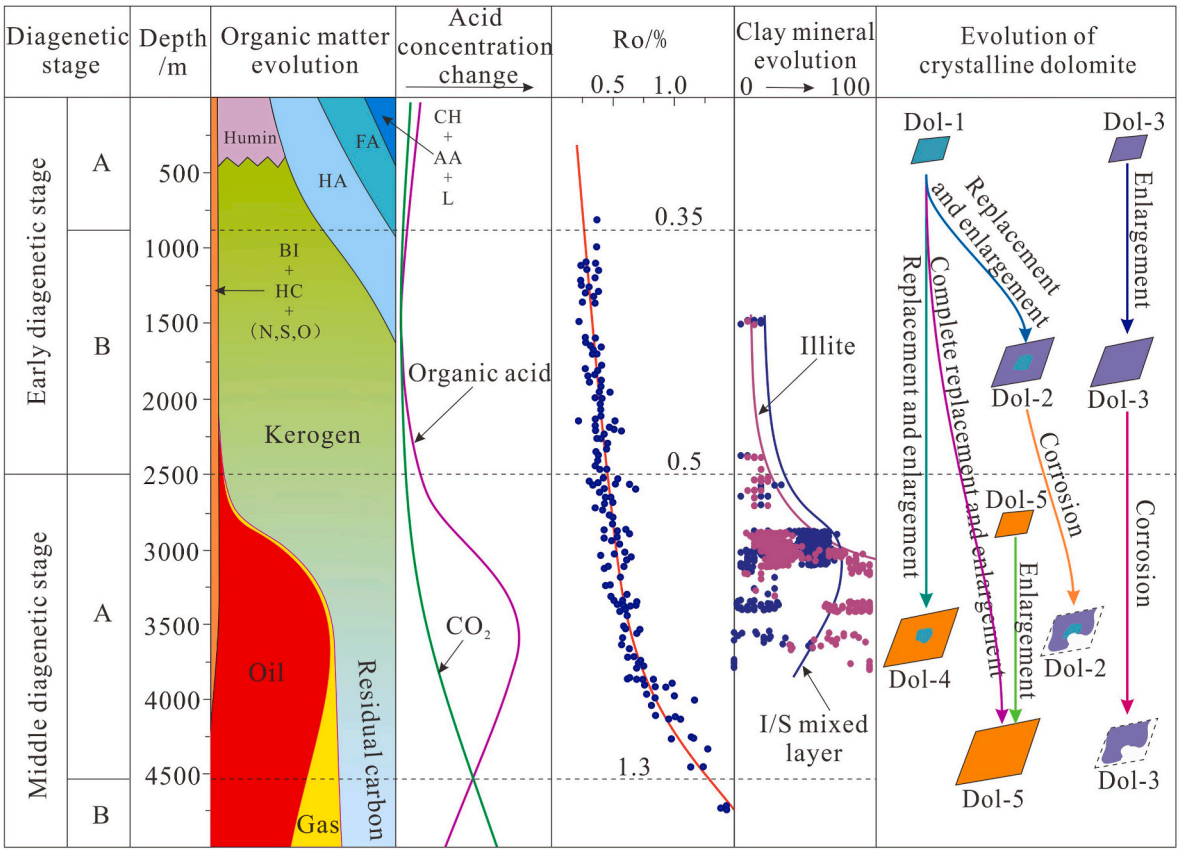

Fig. 13. Diagenetic evolution model of crystalline dolomite.
Note: Thermal evolution characteristics of organic matter were modified from Tissot et al. (1974); Acid concentration changes was modified from Yuan (2015). Ro—Vitrinite reflectance; BI + HC + N, S, O—Inherited bitumen + hydrocarbons + nitrogen, sulfur and oxygen compounds; HA—Humic acid; FA—Fulphic acid; CH—Carbohydrates; AA— Amino acid; L—lipid.

dolomite (FeO < 1%) and the ring-zoning characterized by type II ferroan dolomite (FeO ≈ 16%). The cores are in the shape of cloud, circle and spot, with different sizes, even composed of irregular multiple sub-cores, which have obvious replacement characteristics, indicating that Dol-4 crystalline dolomite is mainly formed by the replacement of early ferroan-poor dolomite by type II ferroan dolomite. Of course, under the condition of sufficient source of Fe-rich diagenetic fluid, the crystals are further enlarged at the same time of replacement.

5.5. Dol-5

Dol-5 crystalline dolomites are distributed in organic-rich laminar mudstone, particularly at the interface (boundary) between clay laminae and organic matter laminae. The euhedral degree of Dol-5 crystalline dolomite is relatively high, mainly rhombic (Fig. 4D), and saddle-shaped can also be observed in phosphorus binding (Fig. 4E), indicating that Dol-5 crystalline dolomite is formed in a high stage of diagenetic evolution. It is also mentioned above that the $\delta^{18}O$ of Dol-5 is between −7.78 and −8.33‰ (Fig. 7), and the corresponding precipitation temperature is between 97 and 101.5 °C. Therefore, Dol-5 crystalline dolomite was formed in the middle diagenetic stage of the maturity period of organic matter. It can be seen from Fig. 3D that Dol-5 crystalline dolomite is associated with Dol-4 crystalline dolomite and columnar ferroan-rich sparry calcite, which proves that Dol-5 should be completely metasomatized by type II ferroan dolomite (FeO ≈ 16%). It can also be seen from Fig. 12H–I that the changes of Ca, Mg, Fe, Sr and Mn elements have basically stabilized from the edge to core, indicating that the composition is relatively uniform after complete replacement. Naturally, Dol-5 crystalline dolomite is further enlarged by the action of diagenetic fluids rich in Fe^{2+}, Mg^{2+} and Ca^{2+}, and new Dol-5 crystalline dolomites will also spontaneously precipitate under the catalysis of clay minerals, as has been proven in previous studies (Liu et al., 2019a; Zhao et al., 2022). For example, Dol-5 crystalline dolomite associated with phosphorus binding, was highly likely to have been directly precipitated by diagenetic fluids (Fig. 4E). Although differences exist in the content of some trace and rare earth elements, such as Tb, in Dol-5 crystalline dolomite compared to the surrounding rock clay minerals (Fig. 8A and B), as well as the phosphorus binding (Fig. 9G–I), the overall distribution trends of trace and rare earth elements in Dol-5 crystalline dolomite are consistent with those observed in the surrounding rock clay minerals (Fig. 8). Generally, the atomic size and charge of Tb also differ greatly from those of Ca, Mg, and Fe, primarily entering ferrodolomite in the form of impurities. However, the high content of Tb in ferrodolomite may be related to the persistent enrichment of diagenetic fluids in the lamellation fractures. As shown in Fig. 9I, Tb is enriched in clay minerals near the lamellation fractures connected to ferrodolomite, which may also be retained by Tb-rich diagenetic fluids flowing along the lamellation fractures. Nevertheless, the distribution trends of their trace and rare earth elements remain largely consistent, indicating that the material compositions of Dol-5 are primarily derived from the material enrichment of the multi-component diagenetic evolution (e.g., clay mineral transformation, early carbonate dissolution), rather than from external fluid injection such as magma intrude. Previous studies have also indicated that small pores, low porosity, tight texture, and low permeability are common characteristics in many shale formations (especially in the study area, the maximum thickness of shale formations exceeds 1 km), facilitating the development of overpressure environments during burial diagenesis (Lahann and Swarbrick, 2011; Zhao

et al., 2017) and limiting the ingress of external diagenetic fluids into the pore system of these rocks (Jarvie, 2012; Xiong et al., 2022). Furthermore, the strontium isotope is a key indicator of the material source, and its value will significantly fluctuate depending on the differences in the sediments due to depositional environment or various hydrothermal fluid source(Taylor et al., 2000; Azmy et al., 2008; Hu et al., 2009). It can be seen from our analysis results that the $^{87}Sr/^{86}Sr$ value is nearly identical to that of micritic dolomite (Fig. 10), which further proves that the material of Dol-5 crystalline dolomite originates from the interior of fine-grained rocks.

In general, Dol-1, Dol-2, Dol-3, Dol-4 and Dol-5 crystalline dolomites were formed in different diagenetic stages. Dol-1, Dol-2, Dol-3 and the core of Dol-4 were formed during the early diagenetic stage, and dominated by ferroan-poor dolomite and type I ferroan dolomite, while Dol-5 and the edge of Dol-4 were formed during the middle diagenetic stage and dominated type II ferroan dolomite.

The crystalline dolomite formed during the early diagenetic stage is related to microbial action and clay mineral transformation, especially microbial action. For example, bacterial action during shallow diagenesis such as sulfate-degrading bacteria (Wright, 1999; Wright and Wacey, 2005; Deng et al., 2010; Bontognali et al., 2012; Krause et al., 2012), methanoic archaea (Roberts et al., 2004; Kenward et al., 2009), fermenting bacteria (Zhang et al., 2015), and various aerobic halophilic bacteria (Rivadeneyra et al., 2006; Sánchez-Román et al., 2008, 2009, 2011; Deng et al., 2010; Balci and Demirel, 2016; Al Disi et al., 2017; Qiu et al., 2017) can effectively catalyze the nucleation and growth of proto-dolomite. According to the euhedral degree, crystal size, dissolution sequence and zoned characteristics of the crystalline dolomite in the study area, most of the crystalline dolomites in the fine-grained rocks precipitated or enlarged in the order of ferroan-poor dolomite–type I ferroan dolomite–type II ferroan dolomite during burial diagenesis. Many researchers also pointed out that the formation of ferroan-rich dolomite is the result of Fe^{2+} replacing the lattice positions of Mg^{2+} and Ca^{2+}, so the ferroan-poor dolomite is generally formed earlier than ferroan-rich dolomite during diagenesis (Huang et al., 2007; He et al., 2010; Liu et al., 2019a). However, we found that, as shown in Fig. 4, there is a non-luminous spot in the core of Dol-2 crystalline dolomite under cathodoluminescence, indicating that ferroan-rich dolomite may also be formed by direct precipitation and crystallization. Although it is extremely uncommon to directly nucleate and form ferroan-rich dolomite in fine-grained rocks, it is not impossible. In fact, experimental studies have also confirmed that sulfate reduction and fermentation can directly lead to the nucleation of ferroan-rich dolomite (Vasconcelos and McKenzie, 1997; Dupraz et al., 2009). In addition, clay minerals with high negative charges such as montmorillonite and illite catalyze abiotic dolomite nucleation through electrostatic interaction of Mg^{2+} and Ca^{2+} and desolubilization of strongly hydrated ions (Liu et al., 2019b).

The type II ferroan dolomite formed during the middle diagenetic stage is related to the transformation of clay minerals and the dissolution of early carbonate. When the organic matter enters a mature stage, the organic acid yield, the dissolution of early carbonate, and the clay mineral conversion rate also reaches a peak (Fig. 13), thus releasing considerable amounts of Ca^{2+}, Fe^{2+}, Mg^{2+}, etc., (Lu et al., 2004; Środoń et al., 2006; Milliken, 2019; Xiong et al., 2022). It is important to note that, with an average relative content of about 80%wt, illite gradually begins to dominate the clay minerals in the Paleogene fine-grained rocks in the research region during the middle diagenetic stage (Fig. 13). The average content of clay minerals in the UMbr 4 is 20.08%wt, and the LMbr 3 is 22.06%wt (Table 1), so the average content of clay minerals in the UMbr 4–LMbr 3 is about 20%wt, and the average absolute content of illite is 16%wt. If the illite is completely transformed from smectite, this evolution process will theoretically release Fe^{2+} about 0.58%wt. Therefore, the transformation of clay minerals has a great contribution to the formation of ferroan-rich dolomite in the research region. These Fe^{2+}-, Mg^{2+}-, and Ca^{2+}- rich fluids will also precipitate and crystallize new ferroan-rich dolomites when replacement or enlargement of early dolomite (Fig. 13).

6. Geological significance

6.1. Diagenetic evolution of fine-grained rocks

Recent research has extensively investigated the diagenesis of carbonate-rich fine-grained rocks (Immenhauser and Rameil, 2011; Liang et al., 2018a,b; Immenhauser, 2021; Xiong et al., 2022), driven by the close relationship between shale oil formation and the diagenetic evolution of these rocks. Different types of crystalline dolomites are the products of fine-grained rocks at different diagenetic stages, which significantly indicates the diagenetic evolution process.

Ferroan-poor and type I ferroan dolomite (e.g., Dol-1, Dol-2 and Dol-3) para- or intergrowed with a substantial amount of framboidal pyrites in organic-rich mudstone primarily related to microbial activity and clay mineral transformation during the early diagenetic stage (Fig. 4J), especially the former. Bacterial sulfide degradation is an important mechanism for the precipitation of these minerals. Ferroan-poor carbonate minerals (ferroan-poor dolomite and calcite) and pyrite will be produced by sulfate-reducing bacteria from hydrated ferric oxides, rather than ferroan carbonate minerals(Curtis, 1978). Ferroan carbonate minerals (ferroan dolomite and calcite) and pyrite will be produced by sulfate-reducing bacteria from ferric hydroxides (Taylor et al., 2000; Roberts et al., 2004; Krause et al., 2012; Zhang et al., 2015; Qiu et al., 2017; Al Disi et al., 2017).

Type II ferroan dolomite, such as Dol-5 and the rim-zone of Dol-4, is associated with large amounts of authigenic microcrystalline quartzs and albites, which is the result of the multi-component diagenetic evolution of fine-grained rocks entering the middle diagenetic stage (Liang et al., 2018a; Xiong et al., 2022). When the shale was buried to the hydrocarbon generation threshold, organic matter undergoes pyrolysis for hydrocarbon generation under the catalytic effect of clay minerals, accompanied by the production of a substantial amount of organic acids. Feldspar and early carbonate minerals were dissolved under the effect of organic acids, especially the dissolution of K-feldspar, which provides a K^{+} source for the clay mineral transformation (e.g., illitization of smectite). The release of products from transformation, dissolution, and evolution resulted in the precipitation of a large amount of microcrystalline quartz, albite, ferrocalcite, and ferrodolomite (Hower et al., 1976; Lynch et al., 1997; Van De Kamp, 2008; Thyberg et al., 2010; Thyberg and Jahren, 2011; Milliken et al., 2016, 2021; Liang et al., 2018a; Milliken, 2019; Xiong et al., 2022).

Additionally, the diagenetic evolution of fine-grained rocks is also confirmed by the symbiotic interactions between various authigenic minerals. As shown in Fig. 4L, Dol-2 crystalline dolomite is wrapped in the sparry calcite, and the sparry calcite has been confirmed to be formed in organic matter maturity period during the middle diagenetic stage (Xiong et al., 2022), indicating that the formation time of ferroan-poor and type I ferroan dolomite is earlier than that of sparry calcite. Furthermore, the evolution of the diagenetic environment in fine-grained rocks is also confirmed by the characteristics of crystalline dolomite. As shown in Fig. 4G, dissolution phenomena of ferroan-poor and type I ferroan dolomite are commonly observed in mudstone, which further indicates that these dolomites were formed in the alkaline environment during the early diagenetic stage, and the diagenetic environment was transformed from the alkaline environment to the acidic environment under the condition that a significant amount of organic acid was released in the later stage, thus leading to dissolution of dolomites formed in the early stage (Fig. 13). The diagenetic environment will be changed from a slightly alkaline environment to a slightly acidic environment once large quantities of organic acids are released in the later stage, resulting in the dissolution of dolomite formed in the early stage (Fig. 13).

6.2. Diagenetic fluid and shale oil migration

The migration of shale oil has always been a hot spot in the study of fine-grained sedimentary petrology (Cardott et al., 2015; Gao et al., 2019; Cui et al., 2022; Huang et al., 2012; Wang et al., 2016). The early focus was to regard shale as source rock, and believed that the migration of oil and gas in the source rock belonged to the category of primary migration (Hao et al., 2000; Li, 2000; Luo, 2003; Jiao et al., 2007; Li et al., 2020; Jin et al., 2021). With the deepening of exploration practice, researchers gradually realized that shale oil reservoirs belong to a whole of source and storage (Wang et al., 2016; Zhang et al., 2019b, 2021). Researchers believe that laminar interfaces and microfractures in shale are the main migration channels for shale oil (Liang et al., 2018a,b). According to the enrichment location of crystalline dolomite, large quantities of authigenic dolomite, calcite and quartz are filled in the laminar interface and microfractures (Fig. 14A), which indeed confirms that these laminar interfaces and microfractures are important migration channels of diagenetic fluid or shale oil. However, we also found that large quantities of crystalline dolomites developed in the granular sparry calcite laminae and the clay laminae (Fig. 14A and B), which also shows that the laminae in fine-grained rocks are also fluid migration channels. In fact, the fine-grained rocks in the Jiyang Depression are characterized by the enrichment of calcite (Table 1), especially in the laminar sparry calcite with large amounts of intercrystalline pores, the maximum diameter exceeding 50 μm (Zhang et al., 2016; Liang et al., 2018a; Shi et al., 2022), so which is an important migration channel for fluids and an important storage space for shale oil. In addition, clay minerals are dominated by I/S mixed layers and illite (Fig. 13), their crystals are characterized by a sheet-like texture distributed along the laminae (Fig. 4D), with good connectivity, so they are also important fluid migration channels.

7. Conclusions

The crystalline dolomites in lacustrine fine-grained rocks are primarily composed of ferroan-poor dolomite (FeO < 1%), type I ferroan dolomite (FeO ≈ 5%) and type II ferroan dolomite (FeO ≈ 16%). The degree of Fe enrichment in crystalline dolomite increases with burial diagenetic evolution. The ferroan-poor dolomite is primarily originated by the microbial action during the early diagenetic stage, while the ferroan-rich dolomite is primarily originated by multi-component evolution (e.g., clay mineral transformation, thermal evolution of organic matter and unstable mineral dissolution) during the middle diagenetic stage. Therefore, the origin mechanism of crystalline dolomite significantly indicates the diagenetic evolution process of fine-grained rocks and migration and enrichment of shale oil.

Although we have analyzed the formation mechanism of crystalline dolomite based on petrology, mineralogy, morphology and geochemistry, the actual underground multi-component diagenetic evolution process is still extremely complicated, and it is hoped that future physical and digital simulations will be realized.

CRediT authorship contribution statement

Zhouhai Xiong: Writing – original draft, Methodology, Investigation, Funding acquisition. **Yingchang Cao:** Supervision. **Chao Liang:** Writing – review & editing.

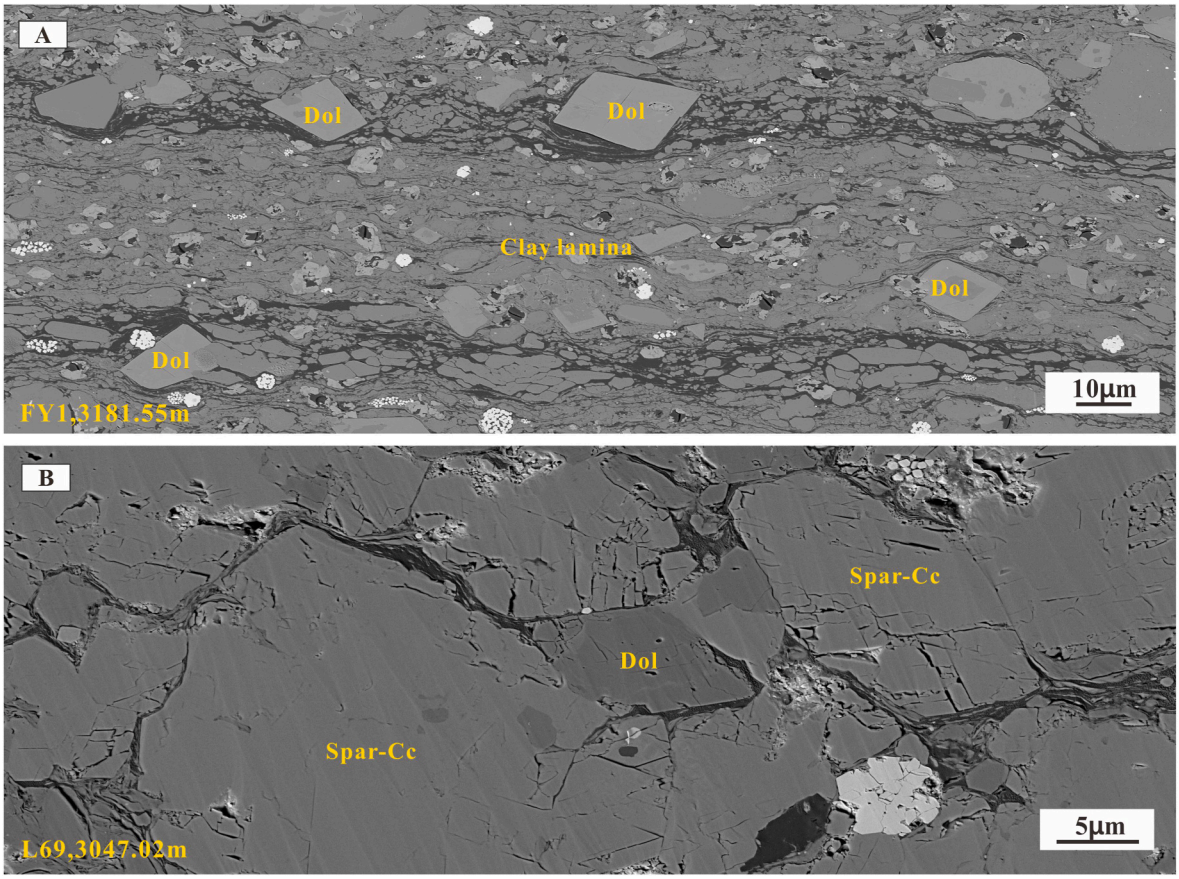

Fig. 14. Crystalline dolomite developed within the laminae.
A. Crystalline dolomite developed within clay lamina, FY1, 3181.55m; B. Crystalline dolomite developed within the lamina of sparry calcite, L69, 3047.02m. Dol—Dolomite; Spar-Cc—Sparry calcite.

Declaration of competing interest

The paper entitled "Characteristics and origin of crystalline dolomite: A case from Paleogene lacustrine fine-grained rocks in Jiyang Depression, Bohai Bay Basin, China", which we wish to be considered for publication in "Marine and Petroleum Geology". No conflict of interest exits in the submission of this manuscript, and manuscript is approved by all authors for publication. I would like to declare on behalf of my co-authors that the work described was original research that has not been published previously, and not under consideration for publication elsewhere, in whole or in part. All the authors listed have approved the manuscript that is enclosed.

Data availability

Data will be made available on request.

Acknowledgements

This study was supported by the National Natural Science Foundation of China (No. U1762217, No. 42302152, No. 42072164, and No. 4182100014), the Natural Science Foundation of Shandong Province (No. ZR2023QD076), the Shandong Provincial Key Research and Development Program (No. 2020ZLYS08), the Taishan Scholars Program (No. TSQN201812030), Qingdao Postdoctoral Application Research Project (No. QDBSH20220202075), and the Fundamental Research Funds for the Central Universities (No. 22CX06010A). We express our sincere gratitude to them.

Appendix A. Supplementary data

Supplementary data to this article can be found online at https://doi.org/10.1016/j.marpetgeo.2024.106694.

References

Adams, J.E., Rhodes, M.L., 1960. Dolomitization by seepage refluxion. AAPG (Am. Assoc. Pet. Geol.) Bull. 44, 1912–1920.
Al Disi, Z.A., Jaoua, S., Bontognali, T.R.R., Attia, E.S.M., Al-Kuwari, H.A.A.S., Zouari, N., 2017. Evidence of a role for aerobic bacteria in high magnesium carbonate formation in the evaporitic environment of Dohat Faishakh Sabkha in Qatar. Front. Environ. Sci. 5, 1–11.
Arvidson, R.S., Mackenzie, F.T., 1999. The dolomite problem: control of precipitation kinetics by temperature and saturation state. Am. J. Sci. 299, 257–288.
Azmy, K., Jin, J., Lavoie, D., Knight, I., Chi, G., 2008. Dolomitization of the Lower Ordovician Aguathuna Formation carbonates, Port au Port Peninsula, western Newfoundland, Canada: implications for a hydrocarbon reservoir. Can. J. Earth Sci. 45, 795–813.
Badiozamani, K., 1973. The dorag dolomitization model, application to the middle Ordovician of Wisconsin. J. Sediment. Res. 43, 965–984.
Bai, Y., Liu, W., Xu, W., 2022. Dolomite genesis and dolomitization mechanisms of the Ordovician lower Yingshan formation, Gucheng area, Tarim basin, China. J. Petrol. Sci. Eng. 215.
Balci, N., Demirel, C., 2016. Formation of carbonate nanoglobules by a mixed natural culture under hypersaline conditions. Minerals 6.
Bojanowski, M.J., 2014. Authigenic dolomites in the Eocene–Oligocene organic carbon-rich shales from the Polish Outer Carpathians: evidence of past gas production and possible gas hydrate formation in the Silesian basin. Mar. Petrol. Geol. 51, 117–135.
Boles, J.R., Franks, S.G., 1979. Clay diagenesis in Wilcox sandstones of Southwest Texas; implications of smectite diagenesis on sandstone cementation. J. Sediment. Res. 49, 55–70.
Boles, J.R., Johnson, K.S., 1984. Influence of mica surfaces on pore-water pH. Chem. Geol. 43, 303–317.
Bontognali, T.R.R., Vasconcelos, C., Warthmann, R.J., Lundberg, R., McKenzie, J.A., 2012. Dolomite-mediating bacterium isolated from the sabkha of Abu Dhabi (UAE). Terra. Nova 24, 248–254.
Budd, D.A., 1997. Cenozoic dolomites of carbonate islands: their attributes and origin. Earth Sci. Rev. 42, 1–47.
Burns, S.J., Baker, P.A., 1987. A geochemical study of dolomite in the Monterey Formation, California. J. Sediment. Res. 57, 128–139.
Carballo, J., Land, L.S., Miser, D.E., 1987. Holocene dolomitization of supratidal sediments by active tidal pumping, Sugarloaf Key, Florida. J. Sediment. Res. 57, 153–165.
Cardott, B.J., Landis, C.R., Curtis, M.E., 2015. Post-oil solid bitumen network in the Woodford Shale, USA- A potential primary migration pathway. Int. J. Coal Geol. 139, 106–113.
Carothers, W.W., Adami, L.H., Rosenbauer, R.J., 1988. Experimental oxygen isotope fractionation between siderite-water and phosphoric acid liberated CO2-siderite. Geochem. Cosmochim. Acta 52, 2445–2450.
Chen, Z., Huang, W., Liu, Q., Zhang, L., Zhang, S., 2016. Geochemical characteristics of the Paleogene shales in the Dongying depression, eastern China. Mar. Petrol. Geol. 73, 249–270.
Claeys, P.F., Mount, J.F., 1991. Diagenetic origin of carbonate, sulfide and oxide inclusions in biotites of the great valley group (Cretaceous), Sacramento valley, California. J. Sediment. Res. 61, 719–731.
Cui, J., Zhang, Z., Liu, G., Zhang, Y., Qi, Y., 2022. Breakthrough pressure anisotropy and intra-source migration model of crude oil in shale. Mar. Petrol. Geol. 135.
Curtis, C.D., 1978. Possible links between sandstone diagenesis and depth-related geochemical reactions occurring in enclosing mudstones. J. Geol. Soc. 135, 107–117.
Davies, G.R., Smith Jr., L.B., 2006. Structurally controlled hydrothermal dolomite reservoir facies: an overview. AAPG (Am. Assoc. Pet. Geol.) Bull. 90, 1641–1690.
Deffeyes, K.S., Lucia, F.J., Weyl, P.K., 1965. Dolomitizanon of Recent and Plio-Pleistocene Sediments by Marine Evaporite Waters on Bonaire netherlands Antilles. The Society of Economic Paleontologists and Mineralogists (SEPM), p. 71.
Deng, S., Dong, H., Lv, G., Jiang, H., Yu, B., Bishop, M.E., 2010. Microbial dolomite precipitation using sulfate reducing and halophilic bacteria: results from Qinghai Lake, Tibetan Plateau, NW China. Chem. Geol. 278, 151–159.
Dupraz, C., Reid, R.P., Braissant, O., Decho, A.W., Norman, R.S., Visscher, P.T., 2009. Processes of carbonate precipitation in modern microbial mats. Earth Sci. Rev. 96, 141–162.
Essene, E.J., Peacor, D.R., 1995. Clay mineral thermometry–a critical perspective. Clay Clay Miner. 43, 540–553.
Friedman, G.M., Sanders, J.E., 1967. Origin and Occurrence of Dolostone, Developments in Sedimentology. Department of Geology, Rensselaer Polytechnic Institute, pp. 267–348.
Friedman, I., Murata, K., 1979. Origin of dolomite in miocene monterey shale and related formations in the Temblor range, California. Geochem. Cosmochim. Acta 43, 1357–1365.
Gao, J.-F., Zhou, M.-F., 2013. Generation and evolution of siliceous high magnesium basaltic magmas in the formation of the Permian Huangshandong intrusion (Xinjiang, NW China). Lithos 162, 128–139.
Gao, Z., Fan, Y., Hu, Q., Jiang, Z., Cheng, Y., Xuan, Q., 2019. A review of shale wettability characterization using spontaneous imbibition experiments. Mar. Petrol. Geol. 109, 330–338.
Given, R.K., Wilkinson, B.H., 1987. Dolomite abundance and stratigraphic age; constraints on rates and mechanisms of Phanerozoic dolostone formation. J. Sediment. Res. 57, 1068–1078.
Guo, J., Zeng, J., Song, G., Zhang, Y., Wang, X., Meng, W., 2014. Characteristics and origin of carbonate cements in the Shahejie Formation of the central uplift belt in the Dongying depression. Earth Sci. J. China Univ. Geosci. 39, 565–576.
Han, Y., He, S., Song, G., Wang, Y., Hao, X., Wang, B., Huo, S., 2012. Origin of carbonate cements in the overpressured top seal and adjacent sandstones in Dongying depression. Acta Pet. Sin. 33, 385–393.
Hao, F., Zou, H., Jiang, J., 2000. Dynamics of petroleum accumulation and its advances. Earth Sci. Front. 7, 11–21.
Hardie, L.A., 1991. On the significance of evaporites. Annu. Rev. Earth Planet Sci. 19, 131–168.
He, Y., Liu, B., Qin, S., 2010. Study on the dolomitization and dolostone genesis. Acta Sci. Nauralium Univ. Pekin. 46, 1010–1020.
Hodell, D.A., Mead, G.A., Mueller, P.A., 1990. Variation in the strontium isotopic composition of seawater (8 Ma to present): implications for chemical weathering rates and dissolved fluxes to the oceans. Chem. Geol. Isot. Geosci. 80, 291–307.
Hower, J., Eslinger, E.V., Hower, M.E., Perry, E.A., 1976. Mechanism of burial metamorphism of argillaceous sediment: 1. Mineralogical and chemical evidence. GSA Bull. 87, 725–737.
Hsü, K.J., Siegenthaler, C., 1969. Preliminary experiments on hydrodynamic movement induced by evaporation and their bearing on the dolomite problem. Sedimentology 12, 11–25.
Hu, Z., Huang, S., Wang, C., Zou, M., Sun, W., 2009. Application of strontium isotope geochemistry to the oil and gas reservoir diagenesis research. Contrib. Geol. Miner. Resour. Res. 24, 160–165.
Huang, S., Qing, H., Hu, Z., Zou, M., Meng, W., Wang, C., Hao, X., Wang, Q., 2007. Closed-system dolomitization and the significance for petroleum and economic geology:An example from Feixianguan carbonates,Triassic NE Sichuan basin of China. Acta Petrol. Sin. 23, 2955–2962.
Huang, Y.-R., Yao, Q.-Z., Li, H., Wang, F.-P., Zhou, G.-T., Fu, S.-Q., 2019. Aerobically incubated bacterial biomass-promoted formation of disordered dolomite and implication for dolomite formation. Chem. Geol. 523, 19–30.
Huang, Z.L., Ma, J., Wu, H.Z., Chen, X., Wen, C., Zhang, J., 2012. Fluid pressure and primary migration characteristics of shale oil of Lucaogou formation in Malang sag. J. China Univ. Petrol. (Ed. Nat. Sci.) 36, 7–11+19.
Immenhauser, A., 2021. On the delimitation of the carbonate burial realm. Depositional Rec. 8, 524–574.
Immenhauser, A., Rameil, N., 2011. Interpretation of ancient epikarst features in carbonate successions — a note of caution. Sediment. Geol. 239, 1–9.
Jarvie, D.M., 2012. Shale resource systems for oil and gas: Part 1—shale-gas resource systems. In: Breye, J.A. (Ed.), Shale Reservoirs—Giant Resources for the 21st Century. AAPG Memoir, pp. 69–87.

Jiang, Z., Xiangxin, K., Yepeng, Y., Zhang, J., Zhang, Y., Li, W., Xiaodong, Y., 2021. Multi-source genesis of continental carbonate-rich fine-grained sedimentary rocks and hydrocarbon sweet spots. Petrol. Explor. Dev. 48, 30–42.
Jiao, Y.Q., Wu, L.Q., He, M.C., Roger, M., Wang, M.F., Xu, Z.C., 2007. Occurrence, thermal evolution and primary migration processes derived from studies of organic matter in the Lucaogou source rock at the southern margin of the Junggar Basin, NW China. Sci. China 50, 114–123.
Jin, Z., Wang, G., Liu, G., Gao, B., Liu, Q., Wang, H., Liang, X., Wang, R., 2021. Research progress and key scientific issues of continental shale oil in China. Acta Pet. Sin. 42, 821–835.
Kaczmarek, S.E., Thornton, B.P., 2017. The effect of temperature on stoichiometry, cation ordering, and reaction rate in high-temperature dolomitization experiments. Chem. Geol. 468, 32–41.
Kenward, P.A., Goldstein, R.H., Gonzalez, L.A., Roberts, J.A., 2009. Precipitation of low-temperature dolomite from an anaerobic microbial consortium: the role of methanogenic Archaea. Geobiology 7, 556–565.
Koeshidayatullah, A., Corlett, H., Stacey, J., Swart, P.K., Boyce, A., Hollis, C., 2020. Origin and evolution of fault-controlled hydrothermal dolomitization fronts: a new insight. Earth Planet Sci. Lett. 541.
Krause, S., Liebetrau, V., Gorb, S., Sánchez-Román, M., McKenzie, J.A., Treude, T., 2012. Microbial nucleation of Mg-rich dolomite in exopolymeric substances under anoxic modern seawater salinity: new insight into an old enigma. Geology 40, 587–590.
Lahann, R.W., Swarbrick, R.E., 2011. Overpressure generation by load transfer following shale framework weakening due to smectite diagenesis. Geofluids 11, 1–15.
Land, L.S., 1985. The origin of massive dolomite. J. Geol. Educ. 33, 112–125.
Land, L.S., 1998. Failure to precipitate dolomite at 25°C fromdilute solution despite 1000-fold oversaturation after 32 years. Aquat. Geochem. 4, 361–368.
Land, L.S., Mack, L.E., Milliken, K.L., Leo Lynch, F., 1997. Burial diagenesis of argillaceous sediment, south Texas Gulf of Mexico sedimentary basin: a reexamination. Geol. Soc. Am. Bull. 109, 2–15.
Li, M., 2000. An overview of hydrocarbon migration research. Petrol. Explor. Dev. 27 (3), 109–117, 10.
Li, M., Jin, Z., Dong, M., Ma, X., Li, Z., Jiang, Q., Bao, Y., Tao, G., Qian, M., Liu, P., Cao, T., 2020. Advances in the basic study of lacustrine shale evolution and shale oil accumulation. Petrol. Geol. Exper. 42, 489–505.
Liang, C., Cao, Y.C., Liu, K.Y., Jiang, Z.X., Wu, J., Hao, F., 2018a. Diagenetic variation at the lamina scale in lacustrine organic-rich shales: implications for hydrocarbon migration and accumulation. Geochem. Cosmochim. Acta 229.
Liang, C., Jiang, Z.X., Cao, Y.C., Wu, J., Wang, Y.S., Hao, F., 2018b. Sedimentary characteristics and origin of lacustrine organic-rich shales in the salinized Eocene Dongying Depression. GSA Bull. 130, 154–174.
Liang, C., Wu, J., Cao, Y., Liu, K., Khan, D., 2022. Storage space development and hydrocarbon occurrence model controlled by lithofacies in the Eocene Jiyang Sub-basin, East China: significance for shale oil reservoir formation. J. Petrol. Sci. Eng. 215.
Liu, H., Zhang, S., Song, G., Xuejun, W., Teng, J., Wang, M., Bao, Y., Yao, S., Wang, W., Zhang, S., 2019a. Effect of shale diagenesis on pores and storage capacity in the Paleogene Shahejie Formation, Dongying depression, Bohai Bay Basin, east China. Mar. Petrol. Geol. 103, 738–752.
Lin, M., Wang, Y., Cao, Y., Wang, S., Xie, Q., Dong, X., 2020. Sources of Ca2+ in the major carbonate cements in Eocene sandstones and conglomerates: Evidence from Sr isotopes, Sr/Ca ratios, and rare-earth elements. Mar. Petrol. Geol. 120, 104568.
Liu, D., Xu, Y., Papineau, D., Yu, N., Fan, Q., Qiu, X., Wang, H., 2019b. Experimental evidence for abiotic formation of low-temperature proto-dolomite facilitated by clay minerals. Geochem. Cosmochim. Acta 247, 83–95.
Lu, X., Liu, Q., Zhang, L., Li, Y., Zhou, R., Lu, J., 2004. Evaluation of the contribution of illitization of smectite to the geopressure in oil-bearing basin. Bull. China Soc. Mineral Petrol. Geochem. 23, 285–291.
Luo, X., 2003. Review of hydrocarbon migration and accumulation dynamics. Nat. Gas Geosci. 14, 337–346.
Lynch, F.L., Mack, E., Land, L.S., 1997. Burial diagenesis of illite/smectite in shales and the origins of authigenic quartz and secondary porosity in sandstones. Geochem. Cosmochim. Acta 61, 1995–2006.
Machel, H.G., 2004. Concepts and models of dolomitization: a critical reappraisal. Geol. Soc., London, Spec. Pub. 235, 7–63.
Mattes, B.W., Mountjoy, E.W., 1980. Burial Dolomitization of the Upper Devonian Miette Buildup, Jasper National Park, Alberta, vol. 28. Society of Economic Paleontologists and Mineralogists, pp. 259–297.
Mazzullo, S.J., 1992. Geochemical and neomorphic alteration of dolomite: a review. Carbonates Evaporites 7, 21–37.
McDonough, W.F., Suna, S.S., 1995. The composition of the earth. Chem. Geol. 120, 223–253.
McKenzie, J.A., Vasconcelos, C., 2009. Dolomite mountains and the origin of the dolomite rock of which they mainly consist: historical developments and new perspectives. Sedimentology 56, 205–219.
Meister, P., Reyes, C., Beaumont, W., Rincon, M., Collins, L., Berelson, W., Stott, L., Corsetti, F., Nealson, K.H., 2011. Calcium and magnesium-limited dolomite precipitation at deep Springs lake, California. Sedimentology 58, 1810–1830.
Milliken, K., Mack, L., Land, L., 1994. Elemental mobility in sandstones during burial; whole-rock chemical and isotopic data, Frio Formation, South Texas. J. Sediment. Res. 64, 788–796.
Milliken, K.L., 2019. Chapter 3: Compactional and Mass-Balance Constraints Inferred from the Volume of Quartz Cementation in Mudrocks. AAPG Memoir, AAPG Special Volumes, pp. 33–48.
Milliken, K.L., Ergene, S.M., Ozkan, A., 2016. Quartz types, authigenic and detrital, in the upper cretaceous eagle ford formation, south Texas, USA. Sediment. Geol. 339, 273–288.
Milliken, K.L., Zhang, T., Chen, J., Ni, Y., 2021. Mineral diagenetic control of expulsion efficiency in organic-rich mudrocks, Bakken Formation (Devonian-Mississippian), Williston Basin, North Dakota, U.S.A. Mar. Petrol. Geol. 127, 104869.
O'Neil, J.R., Clayton, R.N., Mayeda, T.K., 1969. Oxygen isotope fractionation in divalent metal carbonates. J. Chem. Phys. 51, 5547–5558.
Pan, Y., Huang, Z., Li, T., Xu, X., Guo, X., Wang, R., Zheng, H., Zhang, W., 2022. Study on the origin and hydrocarbon generation potential of lacustrine organic-rich dolomite affected by volcanism: A case study of Lucaogou Formation in the Malang Sag, Santanghu Basin, Western China. Mar. Petrol. Geol. 141.
Petrash, D.A., Bialik, O.M., Bontognali, T.R.R., Vasconcelos, C., Roberts, J.A., McKenzie, J.A., Konhauser, K.O., 2017. Microbially catalyzed dolomite formation: From near-surface to burial. Earth Sci. Rev. 171, 558–582.
Potter, P.E., Maynard, J.B., Depetris, P.J., 2005. Mud and Mudstones: Introduction and Overview. Springer Science & Business Media, pp. 157–174.
Qiao, Z.-F., Zhang, S.-N., Shen, A.-J., Shao, G.-M., She, M., Cao, P., Sun, X.-W., Zhang, J., Guo, R.-X., Tan, X.-C., 2021. Features and origins of massive dolomite of Lower Ordovician Penglaiba Formation in the northwest Tarim Basin: Evidence from petrography and geochemistry. Petrol. Sci. 18, 1323–1341.
Qiu, N., Su, X., Li, Z., Liu, Z., Li, Z., 2006. The Cenozoic tectono-thermal evolution of Jiyang depression, Bohai bay basin, East China. Chin. J. Geophys. 49, 1127–1135.
Qiu, X., Wang, H., Yao, Y., Duan, Y., 2017. High salinity facilitates dolomite precipitation mediated by Haloferax volcanii DS52. Earth Planet Sci. Lett. 472, 197–205.
Ramos, F.C., Wolff, J.A., Tollstrup, D.L., 2004. Measuring 87Sr/86Sr variations in minerals and groundmass from basalts using LA-MC-ICPMS. Chem. Geol. 211, 135–158.
Rivadeneyra, M.A., Delgado, R., Párraga, J., Ramos-Cormenzana, A., Delgado, G., 2006. Precipitation of minerals by 22 species of moderately halophilic bacteria in artificial marine salts media: influence of salt concentration. Folia Microbiol. 51, 445–453.
Roberts, J.A., Bennett, P.C., González, L.A., Macpherson, G., Milliken, K.L., 2004. Microbial precipitation of dolomite in methanogenic groundwater. Geology 32, 277–280.
Rodriguez-Blanco, J.D., Shaw, S., Benning, L.G., 2015. A route for the direct crystallization of dolomite. Am. Mineral. 100, 1172–1181.
Rosenbaum, J., Sheppard, S., 1986. An isotopic study of siderites, dolomites and ankerites at high temperatures. Geochem. Cosmochim. Acta 50, 1147–1150.
Sánchez-Román, M., McKenzie, J.A., de Luca Rebello Wagener, A., Rivadeneyra, M.A., Vasconcelos, C., 2009. Presence of sulfate does not inhibit low-temperature dolomite precipitation. Earth Planet Sci. Lett. 285, 131–139.
Sánchez-Román, M., Romanek, C.S., Fernández-Remolar, D.C., Sánchez-Navas, A., McKenzie, J.A., Pibernat, R.A., Vasconcelos, C., 2011. Aerobic biomineralization of Mg-rich carbonates: Implications for natural environments. Chem. Geol. 281, 143–150.
Sánchez-Román, M., Vasconcelos, C., Schmid, T., Dittrich, M., McKenzie, J.A., Zenobi, R., Rivadeneyra, M.A., 2008. Aerobic microbial dolomite at the nanometer scale: Implications for the geologic record. Geology 36.
Shi, J., Jin, Z., Liu, Q., Zhang, T., Fan, T., Gao, Z., 2022. Laminar characteristics of lacustrine organic-rich shales and their significance for shale reservoir formation: A case study of the Paleogene shales in the Dongying Sag, Bohai Bay Basin, China. J. Asian Earth Sci. 223.
Shinn, E.A., Ginsburg, R.N., Lloyd, R.M., 1965. Recent Supratital Dolomite from Andros Island Bahamas. The Society of Economic Paleontologists and Mineralogists (SEPM), p. 112.
Sibley, D.F., Dedoes, R.E., Bartlett, T.R., 1987. Kinetics of dolomitization. Geology 15, 1112–1114.
Środoń, J., Kotarba, M., Biroň, A., Such, P., Clauer, N., Wójtowicz, A., 2006. Diagenetic history of the Podhale-Orava Basin and the underlying Tatra sedimentary structural units (Western Carpathians): Evidence from XRD and K-Ar of illite-smectite. Clay Miner. 41, 751–774.
Taylor, K.G., Gawthorpe, R.L., Curtis, C.D., Marshall, J.D., Awwiller, D.N., 2000. Carbonate cementation in a sequence-stratigraphic framework: Upper Cretaceous sandstones, Book Cliffs, Utah-Colorado. J. Sediment. Res. 70, 360–372.
Teng, J., 2018. Genesis of dolomite in shale drilled by Well Liye1 in Dongying Sag and its significance on sequence boundary indication. Petrol. Geol. Recov. Effic. 25, 1–7+36.
Teng, J., Qiu, L., Zhang, S., Ma, C., 2022. Origin and diagenetic evolution of dolomites in Paleogene Shahejie Formation lacustrine organic shale of Jiyang Depression, Bohai Bay Basin, East China. Petrol. Explor. Dev. 49, 1251–1265.
Thyberg, B., Jahren, J., 2011. Quartz cementation in mudstones: sheet-like quartz cement from clay mineral reactions during burial. Petrol. Geosci. 17, 53–63.
Thyberg, B., Jahren, J., Winje, T., Bjørlykke, K., Faleide, J.I., Marcussen, Ø., 2010. Quartz cementation in Late Cretaceous mudstones, northern North Sea: Changes in rock properties due to dissolution of smectite and precipitation of micro-quartz crystals. Mar. Petrol. Geol. 27, 1752–1764.
Tissot, B., Durand, B., Espitali, J., Combaz, A., 1974. Influence of nature and diagenesis of organic matter in formation of petroleum. AAPG (Am. Assoc. Pet. Geol.) Bull. 58, 499–506.
Vahrenkamp, V.C., Swart, P.K., Purser, B., Tucker, M., Zenger, D., 1994. Late Cenozoic dolomites of the Bahamas: Metastable analogues for the genesis of ancient platform dolomites. Dolomites: Vol. Honour Dolomieu 21, 133–153.
Van De Kamp, P.C., 2008. Smectite-illite-muscovite transformations, quartz dissolution, and silica release in shales. Clay Clay Miner. 56, 66–81.

Vasconcelos, C., McKenzie, J.A., 1997. Microbial mediation of modern dolomite precipitation and diagenesis under anoxic conditions (Lagoa Vermelha, Rio de Janeiro, Brazil). J. Sediment. Res. 67, 378–390.
Wang, Y., Wang, X., Song, G., Liu, H., Zhu, D., Zhu, D., Ding, J., Yang, W., Yin, Y., Zhang, S., Wang, M., 2016. Genetic connection between mud shale lithofacies and shale oil enrichment in Jiyang Depression, Bohai Bay Basin. Petrol. Explor. Dev. 43, 759–768.
Wierzbicki, R., Dravis, J.J., Al-Aasm, I., Harland, N., 2006. Burial dolomitization and dissolution of upper Jurassic Abenaki platform carbonates, deep Panuke reservoir, Nova Scotia, Canada. AAPG (Am. Assoc. Pet. Geol.) Bull. 90, 1843–1861.
Wright, D.T., 1999. The role of sulphate-reducing bacteria and cyanobacteria in dolomite formation in distal ephemeral lakes of the Coorong region, South Australia. Sediment. Geol. 126, 147–157.
Wright, D.T., Wacey, D., 2005. Precipitation of dolomite using sulphate-reducing bacteria from the Coorong Region, South Australia: Significance and implications. Sedimentology 52, 987–1008.
Wu, Z., Li, W., Ren, Y., Lin, C., 2003. Basin evolution in the Mesozoic and superposition of Cenozoic Basin in the area of the Jiyang Depression. Acta Geol. Sin. 77, 280–286.
Xiao, X., Qin, L., Zhang, W., Jiang, X., Xie, J., 2021. The origin of carbonate cements and the influence on reservoir quality of Pinghu Formation in Xihu Sag. Chinese J. Geol. (Scientia Geologica Sinica) 56, 1062–1076.
Xiong, Z., Cao, Y., Liang, C., Liu, K., Wang, G., Zhu, R., Lei, P., Wang, Y., 2022. Origin and significance of authigenic quartz and albite in lacustrine calcareous fine-grained sedimentary rocks. Mar. Petrol. Geol. 143, 105799.
Yang, T., Cao, Y., Friis, H., Wang, Y., Zhou, L., 2018. Diagenetic evolution and chemical changes of deep-water mudstones of Shahejie Formation in the Dongying Sag, Jiyang Depression, Eastern China. Mar. Petrol. Geol. 93, 14–32.
Yuan, G., 2015. Genetic Mechanism of Dissolution of Feldspars and Carbonate Minerals during Diagenesis and its Impact on Reservoir Poroperm. School of Geosciences. China University of Petroleum (East China), Qingdao, pp. 54–60.
Zhang, F., Xu, H., Shelobolina, E.S., Konishi, H., Converse, B., Shen, Z., Roden, E.E., 2015. The catalytic effect of bound extracellular polymeric substances excreted by anaerobic microorganisms on Ca-Mg carbonate precipitation: Implications for the "dolomite problem". Am. Mineral. 100, 483–494.
Zhang, J., Jiang, Z., Jiang, X., Wang, S., Liang, C., Wu, M., 2016. Oil generation induces sparry calcite formation in lacustrine mudrock, Eocene of east China. Mar. Petrol. Geol. 71, 344–359.
Zhang, J., Jiang, Z., Wang, S., Wang, R., Zhang, Y., Du, W., 2021. Bedding-parallel calcite veins as a proxy for shale reservoir quality. Mar. Petrol. Geol. 127.
Zhang, S., Cao, Y., Liu, K., Jahren, J., Xi, K., Zhu, R., Yang, T., Cao, X., Wang, W., 2019a. Characterization of lacustrine mixed fine-grained sedimentary rocks using coupled chemostratigraphic-petrographic analysis: A case study from a tight oil reservoir in the Jimusar Sag, Junggar Basin. Mar. Petrol. Geol. 99, 453–472.
Zhang, S., Liu, H., Liu, Y., Wang, Y., Wang, M., Bao, Y., Hu, Q., Li, Z., Zhang, S., Yao, S., Wang, Y., Xiong, W., Liu, P., Fang, Z., 2020. Main controls and geological sweet spot types in Paleogene shale oil rich areas of the Jiyang Depression, Bohai Bay basin, China. Mar. Petrol. Geol. 111, 576–587.
Zhang, X., Zhang, T., Lei, B., Zhang, J., Zhang, J., Zhao, Z., Yong, J., 2019b. Origin and characteristics of grain dolomite of Ordovician Ma55 Member in the northwest of Ordos Basin, NW China. Petrol. Explor. Dev. 46, 1182–1194.
Zhao, J., Li, J., Xu, Z., 2017. Advances in the origin of overpressures in sedimentary basins. Acta Pet. Sin. 38, 973–998.
Zhao, Z., Dong, C., Ma, P., Lin, C., Li, G., Du, X., Luan, G., He, Y., Liu, W., 2022. Origin of Dolomite in Lacustrine Organic-Rich Shale: A Case Study in the Shahejie Formation of the Dongying Sag, Bohai Bay Basin. Front. Earth Sci. 10.